Prolonged Fluvial Activity From Channel-Fan Systems on Mars

Gaia Stucky de Quay[1,2,3] [ID], Edwin S Kite[1] [ID], and David P. Mayer[1,4] [ID]

[1]Department of the Geophysical Sciences, University of Chicago, Chicago, IL, USA, [2]Department of Earth Science and Engineering, Imperial College London, London, UK, [3]Department of Geological Sciences, Now at University of Texas at Austin, Austin, TX, USA, [4]Now at USGS Flagstaff, Flagstaff, AZ, USA

Abstract Alluvial fans on Mars, which are primarily sourced from erosional alcoves incised into crater rims, record a period of increased surface runoff which ended >1 Ga. However, we lack quantitative constraints on the frequency and duration of river-forming processes and the climatic conditions that accompanied these long-term habitable episodes. Here we use bedrock erosion and sediment transport models to show that the cumulative time span of wet activity (i.e., nonzero erosion and deposition) was between 100 years to 1 Myr excluding dry years. We use Context Camera (CTX) digital elevation models to compile a data set of >200 channels upstream of depositional fans and determine key fluvial geometry metrics. Results from calculating Mars stream power parameters are compared to great escarpment channels and globally distributed bedrock rivers on Earth. Although Martian channel profile morphologies fall within the range of those on Earth, they are slightly less concave-up (concavity index, $\overline{\theta}_\chi = 0.35 \pm 0.16$) and steeper for a given drainage area (reference steepness index, $\overline{k}_{s,\chi} = 0.09 \pm 0.03$, for reference drainage area, $A_r = 1 \times 10^7 \text{ m}^2$). Timescales depend strongly on poorly constrained variables such as erodability and grain size. Channel morphologies, intermittencies, spatial distributions, and orientations collectively suggest an arid climate and a source from snowmelt on steep crater rims, possibly from obliquity-paced insolation variations or orographic accumulation. Derived timescales are consistent with erosion rates and intermittencies observed in arid environments on Earth and do not support short-lived or catastrophic triggers for the warm climate conditions (such as impacts or individual volcanic eruptions).

1. Introduction

On Mars, a suite of incised crater rims sourcing large alluvial fans record a widespread episode of global-scale fluvial activity during the Late Hesperian-Amazonian epochs (Figure 1; Grant & Wilson, 2012; Kraal et al., 2008; Kite et al., 2017; Moore & Howard, 2005). These landforms provide strong evidence that surfaces were modified by liquid water; however, one of the key variables pertaining to ancient hydrological activity on Mars is the timescale over which it operated (Buhler et al., 2014; Hoke et al., 2011; Kite, 2019; Palucis et al., 2014). Obtaining quantitative estimates on the frequency, duration, and spatial distribution of climatic conditions associated with these fluvial landforms can provide important constraints on the time span of habitable climates.

On Earth, alluvial fans occur on tectonically active mountain fronts where a canyon draining from high relief emerges out onto flatter plains (Blair & McPherson, 1994). Martian alluvial fan deposits are similarly bounded by flat, high plateaus and flat crater floors; however, they differ from their terrestrial counterparts in that they are sourced from dendritic channels with high stream orders (i.e., multiple tributaries) located on crater walls instead of mountains (Figures 1b and 1c). As such, both erosional (localized channel alcoves) and depositional (alluvial fans) landforms are preserved and directly linked, forming a closed channel-fan system. In addition, it has been suggested that these systems likely formed due to periodic melting of snow which accumulated on steep crater walls, as opposed to liquid water precipitation (Grant & Wilson, 2012; Morgan et al., 2018).

Channels incised into planetary surfaces are a key record of climatic, lithological, and tectonic signals over space and time (e.g., DiBiase & Whipple, 2011; Ferrier et al., 2013; Goren, 2016; Hack, 1957; Murphy et al., 2016; Perron, 2017; Whipple et al., 1999; Whittaker, 2012; Wobus et al., 2006). Due to the fans' quiescent tectonic setting on Mars, as well as the broadly monolithologic nature of the substrate, the well-preserved
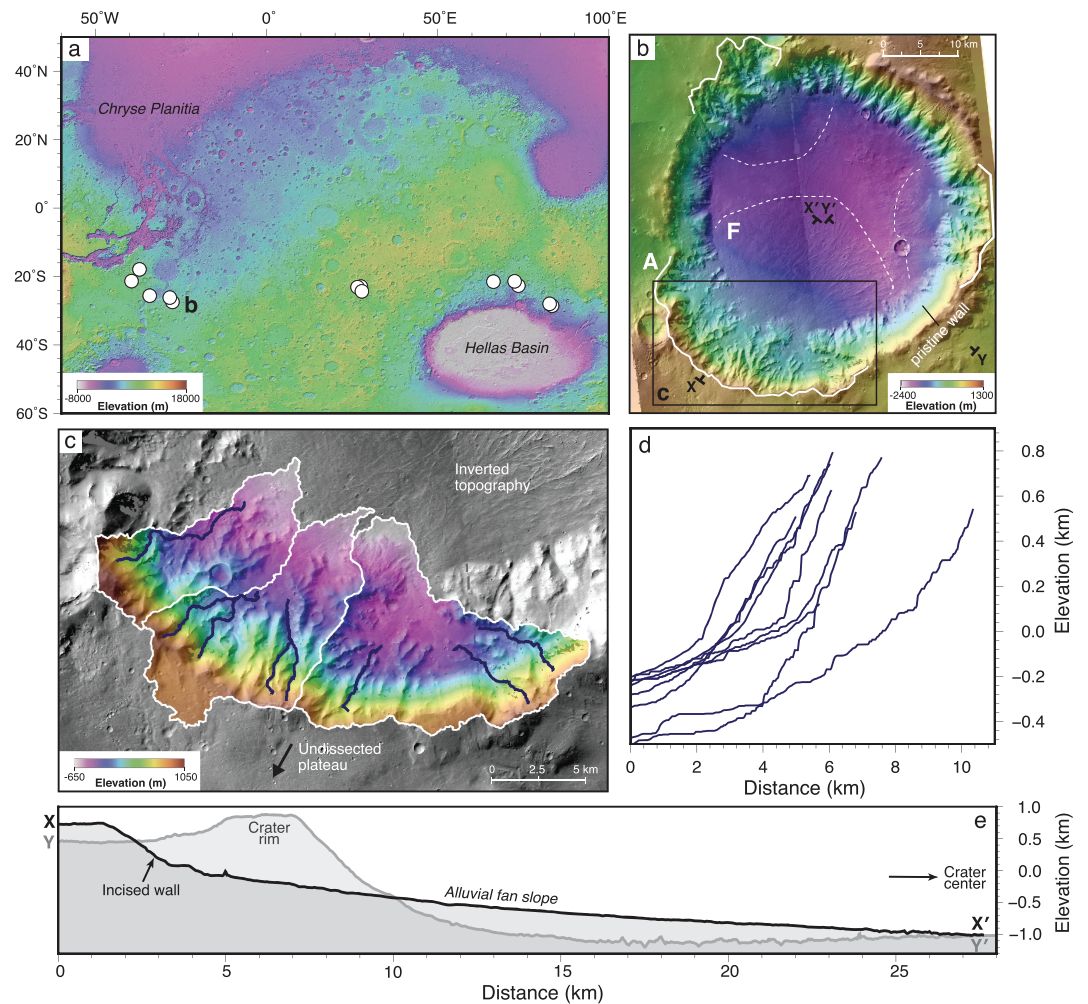
Figure 1. Mapping and extraction of fluvial channels sourcing alluvial fans on Mars. (a) White circles = location of Late Hesperian-Amazonian craters with large alluvial fan deposits and source alcoves from this study; Mars Orbiter Laser Altimeter (MOLA) elevation data. (b) SE Ostrov crater centered at 27°W, 27°S on CTX digital elevation model. White dashed lines = alluvial fan (F) deposit extent; white solid line = incised alcoves (A) on crater rim; black box = extent of panel c. X–X′ and Y–Y′ = transects of cross sections in panel e. (c) Alcove on southeast rim of SE Ostrov crater. White lines = drainage basin; dark blue lines = extracted channels. (d) Longitudinal profiles of channels shown in panel c. (e) Cross sections along incised and nonincised (pristine) crater walls (see panel b).

morphologies of crater rim channels may provide isolated constraints on climate forcing. This forcing is evident from morphological analyses of global channel databases compiled on Earth (e.g., Chen et al., 2019; Harel et al., 2016; Hilley et al., 2019), further implying that climate is likely to be a first-order control on channel-fan system evolution on Mars. Further, since erosion and deposition rates dictate the morphology of landscapes, quantifying key morphometric parameters through topographic analysis enables derivation of fluvial timescales when combined with estimates of rock properties such as grain size or erodability (Roberts et al., 2012; Sklar & Dietrich, 1998; Stock & Montgomery, 1999; Tucker & Whipple, 2002; Whipple & Tucker, 1999).

In this study we build a large data set of CTX (Malin et al., 2007) digital elevation models (DEMs) to assess the morphology and evolution of coupled channel-fan systems on Mars. The preservation of both source and sink landforms allows us to assess their formation conditions and development timescales. To achieve this, we use the stream power law, an erosional model to predict incision rate along a channel (Howard & Kerby, 1983; Rosenbloom & Anderson, 1994; Whipple & Tucker, 1999), as well as sediment transport equations to estimate accumulation rates of fan deposits (Dietrich et al., 2017; Meyer-Peter & Müller, 1948; Pfeiffer et al., 2017). We extract longitudinal profiles of branching source networks for 13 midlatitude craters and

measure morphometric features for a database of >200 channels. We calculate fluvial parameters (channel concavity and steepness indexes) and compare them to terrestrial great escarpments, which comprise steep, kilometer-scale scarps preserved over millions of years (analogous to crater walls), as well as globally distributed bedrock rivers on Earth. This comparison allows us to infer climate factors (e.g., aridity) during the time of channel formation and compare erosion rates and intermittencies to Earth values. Our aim is to derive a range of plausible timescales over which fluvial activity likely occurred by incorporating erosional and depositional models, and to further constrain the climatic conditions and potential origin of observed fluvial environments on Mars.

2. Methodology

2.1. Data

We studied the geomorphology of both alluvial fans and their channelized source alcoves using orbital remote sensing data. We used the National Aeronautics and Space Administration (NASA) Ames Stereo Pipeline (ASP; Beyer et al., 2018) to produce DEMs from CTX stereo pair images with footprints covering the sources and deposits of fan systems (Mayer & Kite, 2016). The 55 DEMs produced have a resolution of 24 m/pixel, and although vertical errors have not been specifically quantified, ASP-generated DEMs generally have errors equivalent to source image pixel scale (i.e., 6 m/pixel; Goudge & Fassett, 2018). We identified 24 individual alcoves (each sourcing its own alluvial fan) located within 13 craters distributed globally (Figure 1a). We used local sinusoidal (equal-area) projections for each system and analyzed the topography using Esri ArcMAP geographic information system. To assess analogous terrestrial escarpment channels, we use NASA Shuttle Radar Topography Mission elevation data (30 m/pixel) and Albers equal-area projection.

2.2. Depositional Measurements

At the apex of each alluvial fan, we measured channel width, slope, and total contributing drainage area for a subset of five fan systems. These metrics are used in section 6 to inform sediment transport models. The widths were measured by identifying positive-relief (inverted) channels in CTX and High Resolution Imaging Science Experiment (HiRISE) images, which represent cemented fluvial sediments exhumed due to differential erosion (see Figures 1b and 1c and supporting information Figure S1; Hayden et al., 2019; Kite et al., 2019; Williams et al., 2007). Local average slope was measured at the fan apex over a distance of 100 m, and drainage area was calculated using total source alcove area (see supporting information Figure S1). We also estimated both alluvial fan volume and the volume eroded from the crater rim by alcove formation. To estimate eroded volume, points were extracted along drainage divides, interfluves, and uneroded crater rims to generate a pre-erosional surface using inverse distance weighting interpolation. This surface was then subtracted from the present topography to determine eroded volume. Similarly for fan deposit volumes, a pre-depositional surface was estimated by extracting and interpolating between points on the pristine crater floor where alluvial fans are not present (supporting information Figure S2). Post-depositional fan erosion is small relative to fan thickness and has negligible effect on fan volume. Note that not all alcoves were included because features were not always measurable (e.g., lack of visible channels and overlapping fan deposits).

2.3. Source Channels: Mapping and Extraction

Using standard flow routing algorithms (fill, flow direction, flow accumulation, and cost path), 10–20 channels were mapped for each alcove (see Figure 1c). Channel heads were identified by setting minimum flow accumulation to 20–50 cells (≈ 1–3×10^4 m^2), and channel mouths were chosen based on where cross-sectional profiles no longer showed a v-shaped valley morphology (i.e., transition from fluvial channel to a resolvable flat-floored or infilled channel; see supporting information Figure S3). V-indexes (a measure of proximity to an ideal v-shaped valley cross section) were calculated along the valleys, with resulting values (<0.1) being consistent with fluvial origin as opposed to glacial or infilled valleys (e.g., Bouquety et al., 2019; Zimmer & Gabet, 2018). Fidelity of channels was checked against 6-m/pixel CTX images, and false positives were removed (e.g., faults and gullies). Channels traced manually were similar in length to digitally extracted channels, which suggests artificial sinuosity from automatic flow routing is negligible. The complete database ($n = 310$) of incised crater rim channels includes measurements of channel head latitude and longitude, length, total drainage area, average slope, channel head elevation, and orientation (supporting information Data Set S1). In addition, we extracted data along each cell of the mapped channel, including coordinates, elevation, downstream (flow) length, upstream drainage area, and data coverage (supporting information Data Set S2). Channels can be plotted to show their longitudinal profiles (i.e., elevation as a

function of distance along a channel) as shown in Figure 1d. These data points along channel length are used to perform stream power analyses to calculate key fluvial parameters for each individual channel as described in the following section.

3. Channel Erosion: Global Stream Power Analysis

3.1. Erosional Parameters

To assess the erosional properties of our incised channel data set, we use the stream power law, an expression for the erosion of fluvial systems. We assume alcove channels are detachment-limited such that their erosion is dictated by the mechanical properties of the substrate (Howard, 1994). The stream power equation is extensively used in terrestrial systems to analyze and interpret bedrock river drainage patterns and their controlling processes. In its simplest form, it is formulated as

$$E = KA^m S^n,$$ (1)

which states that the erosion rate at any point in the river, E, has a power law dependence on the drainage area, A, and channel slope, S (Howard & Kerby, 1983; Rosenbloom & Anderson, 1994; Whipple & Tucker, 1999). K, m, and n are erosional parameters whose values determine the shape of a river and how rapidly a given landscape can evolve. The area and slope exponents, m and n respectively, are empirical constants whose values are unknown and vary over different geological settings. Terrestrial values for m range between 0.3 and 0.8 (with $m = 0.5$ widely used) and n varies between 0.5 and 2, although $n \simeq 1$ is generally used (Paul et al., 2014; Tucker & Whipple, 2002; Whipple et al., 2000). The value of m should only depend on the relationships between (i) discharge and drainage area and (ii) channel width and discharge (Whipple & Tucker, 1999). The value of n controls the propagation of knickpoints (i.e., abrupt changes in gradient resulting in steep channel reaches) along the river network. If $n = 1$, then KA^m corresponds to the knickpoint velocity, and if $n > 1$, then the advective velocity becomes a nonlinear function of local slope and upstream drainage area (Rudge et al., 2015). Although typically termed the erodability, K is thought to be controlled by a complex interaction between climate, precipitation, bedrock lithology, and sediment transport mechanics and is often kept constant over a drainage basin for simplicity (Gallen, 2018; Gasparini et al., 2007; Murphy et al., 2016; Sklar & Dietrich, 1998; Roe et al., 2002; Whittaker, 2012). Previous studies have parameterized these fluvial parameters as a function of climate variability on Earth (Deal et al., 2018; Lague, 2014; Scherler et al., 2017).

We can rearrange equation (1) such that

$$S = \left(\frac{E}{K}\right)^{\frac{1}{n}} A^{\frac{-m}{n}},$$ (2)

which can be further simplified to

$$S = k_s A^{-\theta},$$ (3)

where $k_s = (E/K)^{1/n}$ and $\theta = m/n$. Given that we are able to directly measure A and S remotely from river systems, equation (3) can easily be solved for θ and k_s, which are referred to as the channel concavity and channel steepness indexes, respectively. Importantly, the topographic steady-state assumption (i.e., constant river elevations over time) frequently adopted in this framework to determine rock uplift rates, U, (by simply replacing E by U) is not required and thus not considered in this study (e.g., Harel et al., 2016).

3.2. Slope-Area and Integral Methods

To infer erosion patterns in bedrock river profiles and their geographical variation, θ and k_s are determined using slope-area and χ plots (Perron & Royden, 2013; Schoenbohm et al., 2004). In a slope-area analysis, a linear regression of $\log(A)$ against $\log(S)$ using equation (3) results in a gradient and y intercept corresponding to $-\theta$ and k_s, respectively. Note that this suggests $\log(k_s) = \log(S)$ when $\log(A) = 0$; that is, $A = 1$ m^2. Although θ and k_s are strongly correlated, it is possible to remove their interdependence if equation (3) is rewritten to obtain a nondimensional coefficient by normalizing drainage area by a reference area, A_r (instead of 1 m^2):

$$S = k_{s,r}\left(\frac{A}{A_r}\right)^{-\theta},$$ (4)

where $k_{s,r} = k_s A_r^{-\theta}$ (Sklar & Dietrich, 1998). The value of A_r is selected such that it is centrally located within the drainage area range to facilitate comparison between different tributaries or basins.

However, slope-area analyses are often limited by topographic data and are subject to errors and uncertainty. Differentiating noisy elevation generates significant scatter in slope-area plots, making it challenging to fit a power law trend to data points in order to solve equation (3) with adequate accuracy (Roberts et al., 2012). A more robust method for determining θ and k_s proposed by Perron and Royden (2013) uses elevation, z, instead of slope as the dependent variable, and a spatial integral of drainage area as the independent variable. We can simply integrate equation (2) assuming a simplified setting where E and K are constant in space and time to obtain

$$S = \frac{dz}{dx} = \left(\frac{E}{K}\right)^{\frac{1}{n}} A^{\frac{-m}{n}}, \tag{5}$$

$$\int dz = \left(\frac{E}{K}\right)^{\frac{1}{n}} \int A^{\frac{-m}{n}} dx, \tag{6}$$

where x is the upstream distance. We can substitute in A_r, base-level (at river mouth) $z_b = 0$, *andthe indexes* θ_χ and $k_{s,\chi}$, such that

$$z(x) = k_{s,\chi} \chi, \tag{7}$$

$$\text{with} \chi = \int_{x=0}^{x} \frac{A_r}{A(x)}^{\theta_\chi} dx. \tag{8}$$

Using this method, the river profile's horizontal coordinate is transformed into a variable, χ, which is the upstream distance normalized for drainage area. The steepness indexes from slope-area (k_s) and χ analysis ($k_{s,\chi}$) are closely related, as $k_{s,\chi} = k_s A_r^{-\theta_\chi}$. The identity $k_{s,r} = k_{s,\chi}$ is true if the same reference drainage area A_r is used for both analyses. To determine θ_χ and $k_{s,\chi}$, the θ_χ value which best collapses the river into a straight line, using a linear least squares regression of elevation against χ (i.e., χ space), is selected and the gradient of this line is equivalent to $k_{s,\chi}$. The two methods described above and their resulting plots are illustrated in the following sections where they are assessed in the context of both Mars and Earth bedrock rivers.

3.3. Channels on Mars and Earth

To assess channel concavity and reference steepness indexes of Martian channels, we use slope-area and χ analyses on our channel data set. The assumption of detachment-limited bedrock river behavior is appropriate for our channel extents but is not true further downstream where a transition to alluvial (depositional) processes occur. The channels erode primarily through advection of the crater wall away from the crater center (i.e., retreating in a headward direction; Figure 1e). This is supported by the persistence of sharp crater rims suggesting diffusive processes are negligible (see Figures 1b, 1c, and 1e). There is no evidence for post-fluvial or syn-fluvial tectonic modification implying $U \sim 0$. Crater walls containing channels have retreated 5–20 km relative to uneroded walls (Figure 1c,e) and are thus not in steady-state; however, Royden and Perron (2013) demonstrated that even in cases of transient channel incision the slope in χ space ($= k_{s,\chi}$) will still reflect local erosion rates. Further, although there is no uplift-erosion balance for these channels, a river profile can still achieve equilibrium or quasi-equilibrium through variations in sediment grain size or feedback from upstream landsliding (Egholm et al., 2011; Howard et al., 2016; Sinha & Parker, 1996). Thus, crater rim river profiles could preserve a steady-state profile in a crater rim/drainage divide reference frame, despite not being classically in steady-state.

We also note that equations (4–6) assume constant A and E over time. We acknowledge that A should increase over time, but as we are considering only the upper reaches of tributaries these changes are small. Further, temporally constant drainage areas have been used in previous terrestrial models to derive realistic erosion rates (e.g., Roberts et al., 2012; Rudge et al., 2015). The erosion rate E represents a mean value during total erosional timescale (from channel incipience to abandonment). Figure 2 illustrates three example channels for which the fluvial parameters (channel concavity and reference steepness indexes) were calculated.

In order to compare the observed concavity and steepness indexes on Mars to terrestrial counterparts, channels were also mapped and extracted from the three largest well-preserved escarpments on Earth: Serra
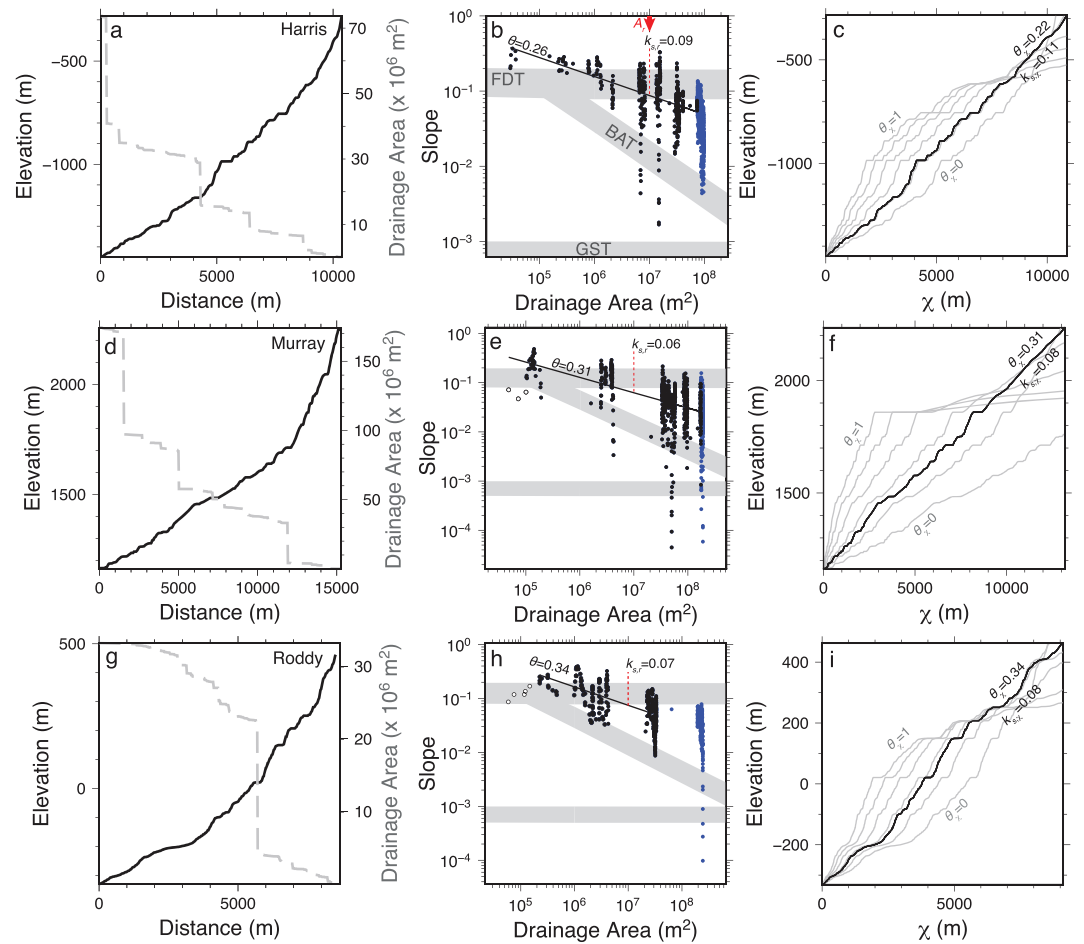
Figure 2. Calculation of channel parameters using slope-area and χ plot analyses for three example channels in Harris, Murray, and Roddy craters. (a, d, and g) Black line = channel longitudinal profile, dashed gray line = drainage area. (b, e, and h) Slope-area plots to find concavity index, θ, and reference steepness index, $k_{s,r}$, for reference drainage $A_r = 1 \times 10^7$ m^2 (red arrow); black circles = river points (24-m increment; 500-m Gaussian filter) used in this study; black line = best fit slope; white circles = points upstream of hillslope-channel transition; blue circles = points downstream of end of v-shaped valley. Gray bands = location of transition zones of fluvial processes on Earth from Sklar and Dietrich (1998). FDT = fluvial-debris flow transition, where debris flows occur above and fluvial processes below. BAT = bedrock-alluvial transition, where alluvial rivers occur to the left and bedrock rivers to the right. GST = gravel-sand transition, where sand sediment is predominant below and gravel above. (c, f, and i) χ analyses for multiple values of θ_χ. Black line = best fitting θ_χ; gray lines = χ curves for θ_χ at 0.2 intervals. Slope of black line = $k_{s,\chi}$.

Geral in Brazil, Great Escarpment in western South Africa, and the Western Ghats in India (see Figure 3; Matmon et al., 2002). The escarpment morphologies have sustained millions of years of erosion mainly through headward retreat after stabilization following rifting and expansion from seafloor spreading (Braun, 2018; Ollier, 1985). These scarps are excellent analogs for retreating Martian crater rims due to their (i) quiescent tectonic setting in present-day passive margins, (ii) drainage divides that coincide with scarp rims, (iii) exceptional preservation of scarp rims over geological timescale, suggesting advective retreat is the predominant erosional process, (iv) morphologies defined by a steep slope bounding upper and lower horizontal plateaus ~1 km in elevation difference, (v) channel networks that cut into scarp bedrock generating localized alcoves with comparable flow lengths (~10 km), and (vi) predominantly basaltic lithologies. No other terrestrial systems (e.g., volcanoes or meteor craters) exhibit all these characteristics simultaneously. Lastly, we also include parameters calculated from a global compilation ($n = 1,456$) of bedrock rivers from Harel et al. (2016). These rivers span a variety of climatic, lithologic, and tectonic settings and were obtained using the same techniques. We note, however, that flexural isostasy plays an important role in terrestrial escarpment evolution (e.g., Braun, 2018; Braun & Beaumont, 1989; Tucker & Slingerland, 1994; van der Beek et al., 2002) and less so on Mars (elastic thickness $T_e > 60$ km; McGovern et al., 2002; Ruiz, 2014). The results for
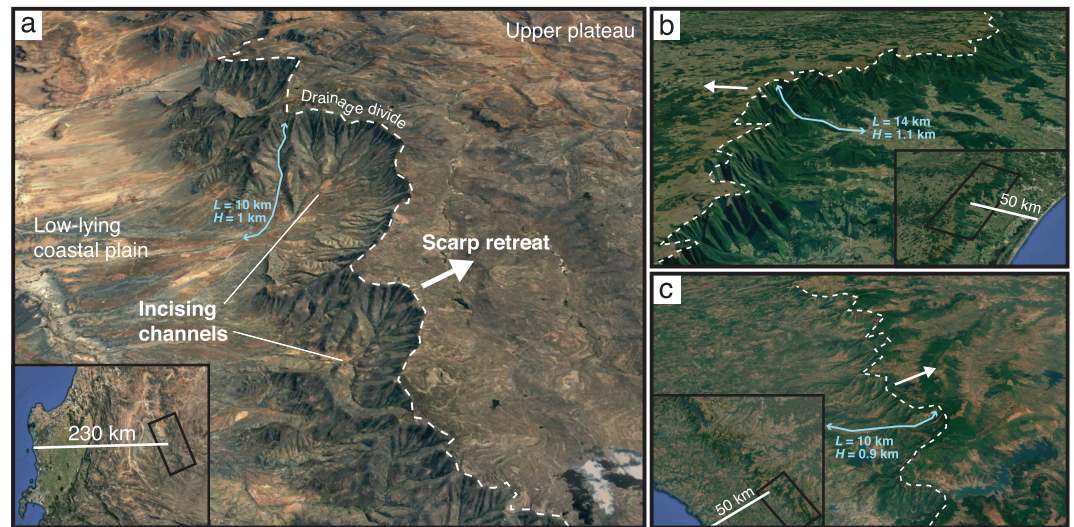
Figure 3. Examples of great escarpments on Earth as analogs for Martian crater rim erosion. Insets show location of scarps relative to coast (scarp origin point). Light blue line = example channel for scale (L = length, H = height difference). White dashed line = scarp rim and drainage divide. (a) Great Escarpment in western South Africa (32°28′ S, 20° 23′ E). (b) Serra Geral, Brazil (28° 47′ S, 49° 54′ W). (c) Western Ghats, India (16° 25′ N, 73° 48′ E). Imagery was extracted from GoogleEarth using 3 times vertical exaggeration.

calculated parameters for all three data sets (Martian crater rim, terrestrial scarps, and bedrock rivers) are presented in the following section.

4. Results

4.1. Slope-Area Relations

The extracted channels on Mars display concave-up (graded) longitudinal profiles (Figures 2a, 2d, and 2g). Application of stream power analyses indicates a strong relationship between S and A and well-defined concavity and steepness indexes with little variation between slope-area and χ methods (Figure 2 and supporting information Figure S4). Channel data points exclude any values beyond the "rollover" shown in Figures 2e and 2h where S no longer depends on A and hillslope processes dominate over fluvial incision. Note that Mars data points generally fall within Sklar and Dietrich's (1998) fluvial, bedrock zones which dictate where stream power law is broadly applicable for a given value of slope and drainage area (i.e., below the fluvial-debris flow transition [FDT], and to the right of the bedrock-alluvial transition [BAT]; Figures 2b, 2e, and 2h). Our data points cross debris flow and alluvial transitions near the channel head and mouth respectively, an observation consistent with our channel boundary definitions in section 2.3 (Conway et al., 2011). Finally, to reduce outliers and sources of topographic noise, we removed channels which showed either one of the following characteristics: (i) an r^2 value of < 0.97 from poor linear fits in χ space due to large knickpoints or topographic noise; (ii) a Gini coefficient of <0.1 (i.e., convex-up rivers); or (iii) river lengths <4 km due to low signal:noise (see supporting information Figure S4). The resulting subset of Mars channels (n = 216; supporting information Data Set S1) and their calculated fluvial parameters are compared to terrestrial counterparts in the following subsection.

4.2. Channel Concavity and Steepness Index Comparison

The values obtained for channel concavity and steepness indexes are shown in Figure 4. For simplicity, we consider only the channel concavity and steepness indexes derived from the χ method (θ_χ, $k_{s,\chi}$) due this method's increased reliability compared to the slope-area method. Channel concavities typically range between 0.1 and 0.5, with a mean and standard deviation $\overline{\theta}_\chi$ = 0.35 ± 0.16. Reference steepness indexes have a narrower range defined by a mean and standard deviation $\overline{k}_{s,\chi} = 0.09 \pm 0.03$. We included parameter values derived for the three great escarpments on Earth. Generally, all three systems have higher concavities $\theta_\chi > 0.5$ and similar or lower $k_{s,\chi}$ values. The full global data set of bedrock rivers from Harel et al. (2016) is included, with rivers classified as belonging to active or nonactive tectonic settings. The average concavity index for terrestrial rivers is $\theta_\chi \simeq 0.5$ for both active and nonactive settings. However, Figure 4 shows that
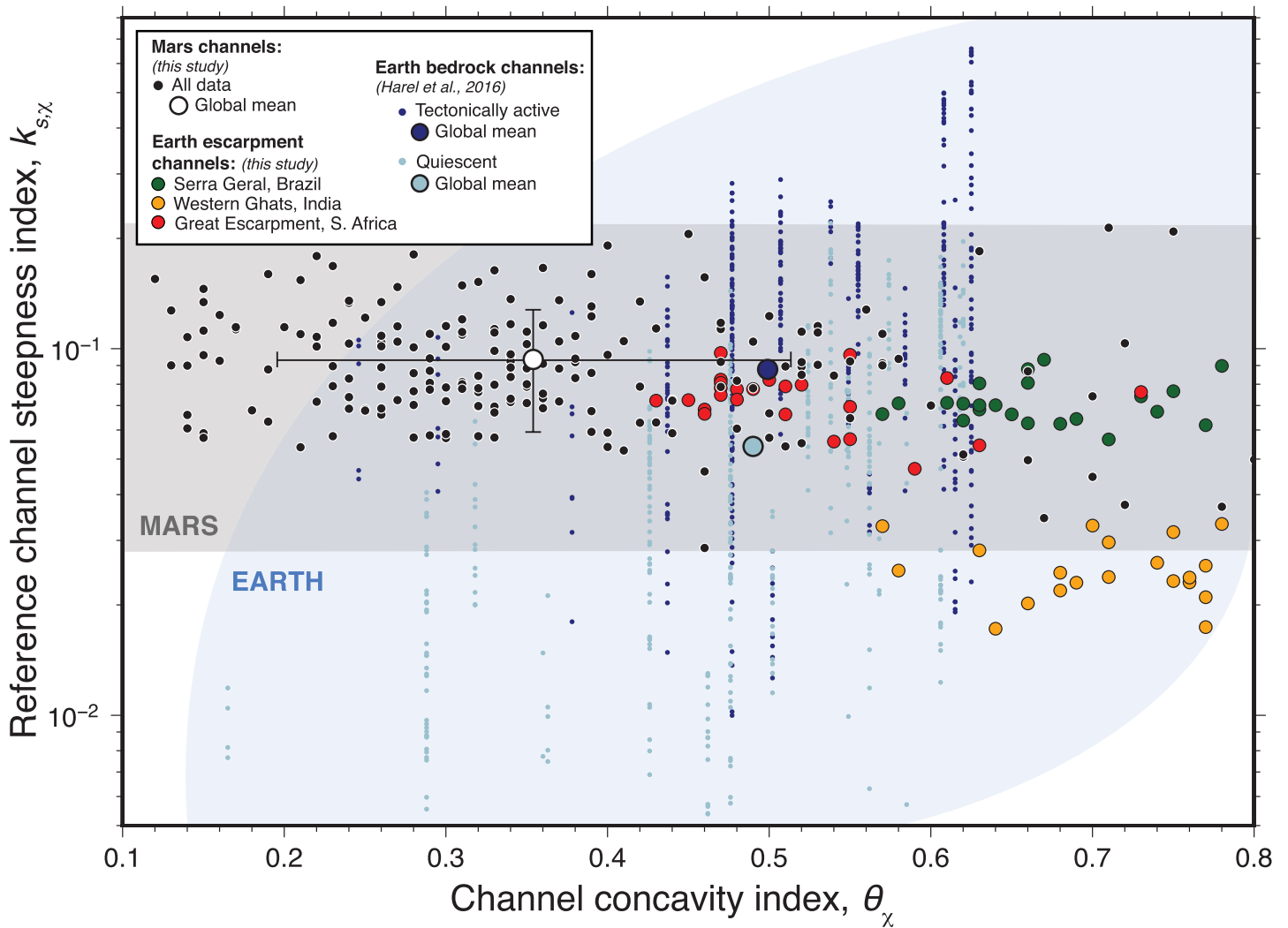
Figure 4. Channel concavity index θ_χ, and reference channel steepness index, $k_{s,\chi}$ ($A_r = 1\times10^7$ m^2), on Earth and Mars. Black circles = crater rim channels sourcing alluvial fans on Mars collected in this study; white circle = mean ±1σ. Colored circles represent various terrestrial channels from this study and from Harel et al. (2016; escarpment channels and bedrock rivers channels; see figure key). Blue/gray colored bands = all data points within Earth/Mars. See text for explanation of bedrock channel data point distribution. Note logarithmic scale on y axis only.

rivers in tectonically active regions on Earth can have $k_{s,\chi}$ values almost an order of magnitude higher than those on Mars ($\sim$0.7), while quiescent regions have values over an order of magnitude lower (<0.006).

The Harel et al. (2016) data set shows the following three characteristics: (i) Their θ values are (deliberately) cutoff above $\sim$ 0.65; (ii) to calculate a normalized $k_{s,\chi}$ they use a basin-averaged θ_χ, which is evident from observing that data points in Figure 4 cluster over specific concavities, where each group represents a basin. Although this methodology is suggested by Perron and Royden (2013) as a means of comparing channel steepness indexes within a drainage basin, our goal is to explore the variability of both parameters for each channel at a global scale, and thus, this method was not employed (resulting in scattering of θ_χ on Mars); (iii) the slight positive correlation between θ_χ and $k_{s,\chi}$ in their data most likely stems from our choice of reference drainage area, which was chosen to be central over our comparatively smaller <20-km channels with lower drainage areas and is less effective at normalizing their data points (see section 3.2). Notably, fluvial parameters θ_χ and $k_{s,\chi}$ for Mars channels show no clear correlation with other geographical variations such as elevation, latitude, orientation, or fan deposit thickness. Additionally, we found that as Mars channels increase in length, the scatter in θ_χ and $k_{s,\chi}$ decreases and values converge toward the global means (supporting information Figure S5). This suggests that the parameter values are appropriate constant approximations for channels sourcing alluvial fans and that calculated scatter may originate from

Table 1
Key Morphometric Values for a Subset of Five Alcove/Fan Systems Used to Derive Fluvial Timescales (See Supporting Information Figure S1 and Table S1)

Crater, alcove	Alcove			Alluvial channel	
	Latitude/Longitude (°)	Area, A_A (m^3)	Volume, V_A (m^3)	Width, w (m)	Slope, s (m/m)
SE Saheki, S	−23.434, 74.330	1.2×10^8	3.5×10^{10}	80	0.05
Harris, N	−21.406, 67.186	3.6×10^7	6.7×10^9	50	0.06
Murray, S	−23.900, 28.138	1.9×10^8	5.3×10^{10}	120	0.05
Holden, S	−27.052, −34.462	9.7×10^7	2.2×10^{10}	50	0.06
Roddy, N	−21.538, −39.935	1.1×10^8	3.3×10^{10}	150	0.05

decreased signal:noise for shorter channels. The well-constrained fluvial constants can be combined with terrestrial erodability values to infer a plausible range of erosion rates and erosional timescales, which we explore in the following section.

5. Erosion Timescales

In order to explore the timing of fluvial activity, we use the relationships established in previous sections where $k_{s,\chi} = k_s A_r^{-\theta_\chi}$ and $k_s = (E/K)^{1/n}$ (see section 3.2). We combine these two relations to derive an expression for the erosion rate such that

$$E = K(k_{s,\chi} A_r^{\theta_\chi})^n. \tag{9}$$

To solve for E, we use the global averages of $\overline{k}_{s,\chi} = 0.09 \pm 0.03$ and $\overline{\theta}_\chi = 0.35 \pm 0.16$ for Mars channels from Figure 4. Given a range of K and n, we can obtain a range of erosion rates. Since E is denudation rate, dz/dt, we can combine the expression in equation (9) with the amount of denudation, z_A, derived from the alcoves to determine the total timescales needed for erosion to occur, assuming a constant S and A for simplification. Table 1 lists morphometric parameters measured for a subset of five alcoves (see section 2.2). Using the total area of the alcove, A_A, and the estimated volume eroded from the crater rim, V_A, we find the total basin-averaged denudation, $z_A = V_A/A_A$. Using the mean denudation for all alcoves ($z_A = 260$ m; Table 1), we obtain an expression for total erosional timescale, T_E, as a function of K and n:

$$T_E(K, n) = \frac{\overline{z}_A}{K(\overline{k}_{s,\chi} A_r^{\overline{\theta}_\chi})^n}, \text{ or} \tag{10}$$

$$T_E(K, n) = \frac{260\,\text{m}}{K \times 0.09^n \times (10^7\,\text{m}^2)^{0.35n}}, \tag{11}$$

where K has units (meters)$^{1-2m}$ per year and T_E has units of years. Figure 5 presents the range of possible erosional timescales given the span of K values observed on Earth and various n parameters (Campforts & Govers, 2015; Czarnota et al., 2014; Stock & Montgomery, 1999; Whipple & Tucker, 1999). The total envelope of expressions include $\pm 1\sigma$ for θ_χ and $k_{s,\chi}$. The highest erodabilites suggest timescales of <1 year, whereas lower erodabilities indicate timescales >10^4 years. Note that values $K \sim 10^{-2}$ m$^{0.2}$ year^{-1} are generally found in mudstones, while $K = 10^{-5}$–10^{-6} and $< 10^{-6}$ m$^{0.2}$ year^{-1} are observed for volcaniclastic and metamorphic/granitic lithologies, respectively (for m=0.4; Stock & Montgomery, 1999). For example, for modern bedrock rivers incising into columnar basalts sourced from glacial meltwater in Iceland, erodability was calculated as 8×10^{-6} year^{-1}, roughly equivalent to $T_E = 10^3$–10^7 years in Figure 5 (for m=0.5; Stucky de Quay et al., 2019). The relative importance of rock strength and precipitation in parameterizing K is poorly constrained even on Earth, although the dependence of erosion rate on tensile strength has been directly observed in the lab (Ferrier et al., 2013; Sklar & Dietrich, 2001). Although constraints on compressive rock strength on Mars exist (e.g., Peters et al., 2018; Thomson et al., 2013), we require a better quantitative understanding of how these directly relate to tensile strength and river incision.

Timescale differences between the five alcoves are nonresolvable in the plot due to small variation in denudation between them, consistent with near equivalent formation times for all separate systems. Due to the closed sediment budget observed for each system (erosional alcove paired with depositional alluvial fan), we can further examine fluvial timescales by considering sediment transport models to shed light on the amount of time required to generate these landforms.
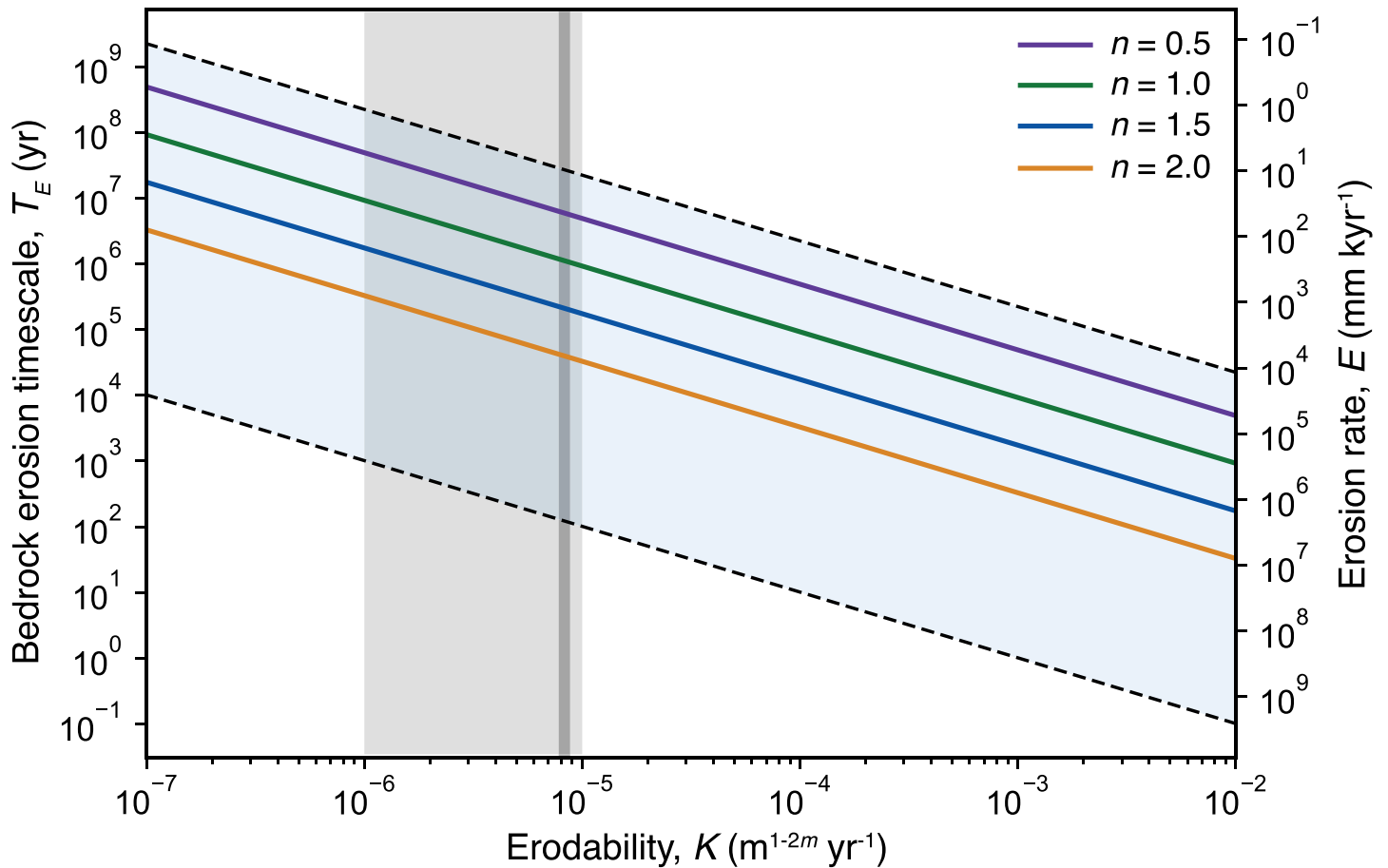
Figure 5. Erosion rates for bedrock channels and timescale of alcove formation as a function of rock erodability, K, using average Martian reference channel steepness ($\bar{k}_{s,\chi} = 0.09$) and concavity index ($\bar{\theta}_{\chi} = 0.35$) from Figure 4. Colored lines = varying n parameters typically used on Earth (Whipple et al., 2000). Dashed black lines = upper and lower boundaries incorporating $\pm 1\sigma$ for both $k_{s,\chi}$ and θ_{χ} values. Blue band = region enclosing possible values within given parameters and errors. Dark gray band = K from bedrock erosion over columnar basalts in Iceland ($8.3 \pm 0.5 \times 10^{-6}$ year^{-1}; Stucky de Quay et al., 2019). Light gray band = K for volcaniclastic rocks (Stock & Montgomery, 1999). Range of K was chosen to represent values observed on Earth (10^{-7}–10^{-2} m$^{0.2}$ year^{-1}; Campforts & Govers, 2015; Stock & Montgomery, 1999). Note that K values incorporate terrestrial intermittent bankfull discharge.

6. Sediment Transport Timescales

In the previous section we derived timescales required to incise bedrock channels using stream power relations and globally averaged fluvial parameters. The preservation of fans downstream allow us to also estimate timescales by applying sediment transport relationships required to build these alluvial deposits. We examine the same five systems listed in Table 1 using values estimated from alluvial fan apexes. We use three different methods to calculate sediment discharge and total time required to transport the known sediment volume.

6.1. Method 1: Snowmelt RunOff and Open Channel Friction Flow

6.1.1. Paleohydrological Constraints

In our first method, we initially estimate the water discharge within alluvial channels using runoff constraints and combine these with established sediment transport equations to infer sediment discharges. Water discharge, Q_w, is expressed as

$$Q_w = uhw, \tag{12}$$

where h = cross sectionally averaged water depth, w = channel width, and u = average flow velocity. The width is derived from imagery and was measured for sites listed in Table 1. For Martian channels, flow depths are challenging to constrain, particularly in the absence of incised canyon walls or terraces. Instead, we derive an expression for h using estimates for water discharge. We find Q_w using the energy balance in

Kite et al. (2013) where runoff, r_o, from snowmelt due to insolation has an energetic upper limit of 3 mm/hr on Mars (section 7.3). Using a drainage area relationship where

$$Q_w = r_o A_A, \tag{13}$$

we can then combine equations (12) and (13) to obtain an expression for flow velocity:

$$u = \frac{r_o A_A}{hw}, \tag{14}$$

where total upstream drainage areas for each alcove, A_A, are listed in Table 1. Here we assume the catchment simultaneously melts and produces a steady runoff rate and Q_w (Palucis et al., 2014).To constrain flow conditions, we evaluate an open channel method, which assumes steady, uniform (constant depth) flow in a channel that has a rigid boundary (i.e., flow conditions up to bed motion; Williams & Irwin, 2009). The Manning equation, a friction law which incorporates resistance coefficients and channel geometry, takes the form

$$u = 8\sqrt{ghs}\left(\frac{h}{\kappa_s}\right)^{1/6}, \tag{15}$$

where g is gravitational acceleration, s is channel slope, and κ_s is the hydraulic roughness length commonly related to some grain size percentile (Parker, 1991). For flows that are much wider than deep ($w \gg h$), h is used in place of the hydraulic radius (cross-sectional flow area divided by the wetted perimeter) generally required for open channel flow (Coleman, 2015). We incorporate the value D_{84}, the grain size for which 84% of the particles sizes are smaller, in our hydraulic roughness such that $\kappa_s = 3.5 D_{84}$ (e.g., Palucis et al., 2014). Channel geometries (w and s; Table 1) are assumed to be constant during channel-forming periods, which is supported by the low variability of w within each fan system and a narrow range of observed s ($= 0.05$ or 0.06). To solve for the flow depth, we equate (14) and (15) to obtain the expression:

$$h = \left(\frac{\kappa_s^{1/6} r_o A_A}{8w\sqrt{gs}}\right)^{3/5}. \tag{16}$$

6.1.2. Sediment Transport and Deposition

Having constrained water column height derived from snowmelt, we can determine sediment discharge by calculating bedload transport rates, which are generally expressed as being related to excess dimensionless shear stress raised to some power (Kleinhans, 2005). The dimensionless shear stress, τ^*, or Shields parameter, represents the ratio of hydrodynamic forces acting on the bed to the submerged weight of the particles:

$$\tau^* = \frac{\tau_b}{R\rho_w g D_{50}}, \tag{17}$$

where bed shear stress $\tau_b = \rho_w ghs$, submerged specific gravity $R = (\rho_s - \rho_w)/\rho_w$, and ρ_w and ρ_s are water (1,000 kg/m³) and sediment (3,000 kg/m³) densities, respectively. We substitute $D_{50} = 0.5 D_{84}$ for median grain size (Recking, 2012). We incorporate the expression for h from equation (16) to find τ^*. To calculate sediment transport, we use the Meyer-Peter and Müller equation, which is related to the excess of the Shields stress above some appropriately defined critical Shields stress, τ_c^*:

$$Q_s = 8w\sqrt{RgD_{50}^3}(\tau^* - \tau_c^*)^{3/2}, \tag{18}$$

where Q_s is volumetric sediment discharge integrated over unit channel width, w (Meyer-Peter & Müller, 1948). The critical bed shear stress typically varies between 0.03 and 0.08 but can be expressed as a function of the slope such that $\tau_c^* = 0.15 S^{0.25}$ (Buffington & Montgomery, 1997; Lamb et al., 2008; Morgan et al., 2014).

Finally, given an eroded alcove volume V_A (Table 1), we can then determine the fan formation timescale from sediment transport $T_{T,1}$ since $T_{T,1} = V_A/Q_s$. Equations (16)–(18) can be combined to derive an expression for $T_{T,1}$ as a function of the unknown parameter: grain size (D_{84}). It can be written as

$$T_{T,1}(D_{84}) = \frac{c_1}{\left(c_2 D_{84}^{-9/10} - c_3\right)^{3/2} D_{84}^{3/2}}, \text{ where} \tag{19}$$

$$c_1 = \frac{V_A}{8w\sqrt{Rg/8}},$$

$$c_2 = \frac{2s}{R}\left(\frac{3.5^{1/6}r_o A_A}{8w\sqrt{gs}}\right)^{3/5},$$

$$c_3 = \tau_c^*.$$

Note that since estimated r_o is a maximum value, this method provides a minimum formation timescale for our values.

6.2. Methods 2 and 3: Terrestrial Gravel-Bedded River Databases

6.2.1. Bed/Critical Shear Stress (τ^*/τ_c^*) Ratio

A second method for estimating sediment transport timescales is used which does not require an assumption of maximum runoff generated from snowmelt. Instead, we use a compilation of bed shear stress to critical shear stress ratios (τ^*/τ_c^*) measured for >300 gravel-bed rivers from across North America from Pfeiffer et al. (2017; e.g., Kite et al., 2019). This ratio is referred to as the transport stage, ϕ, and is important in that it shows bed shear stress as a multiple of the value of the criterion for initiation of motion. The measured ϕ values are centered on $\overline{\phi} = 2.0 \pm 1.6$ for all measured rivers. We take this mean and standard deviation and combine equation (18) to find Q_s and derive an expression for sediment transport timescales $T_{T,2}$ as a function of D_{84}:

$$T_{T,2}(D_{84}) = \frac{V_A}{8w\sqrt{Rg/8}(\overline{\phi}\tau_c^* - \tau_c^*)^{3/2}}\frac{1}{D_{84}^{3/2}}. \tag{20}$$

6.2.2. Sediment/Water Discharge (Q_s/Q_w) Ratio

Lastly, we use a compilation of sediment to water discharge ratios (Q_s/Q_w) obtained from 411 gravel-bedded rivers on Earth from Dietrich et al. (2017). We denote these measured values as sediment concentration, C, where $\overline{C} = 10^{(-3.28\pm0.92)}$. As with Method 1, we assume a Q_w that is energetically limited by snowmelt-sourced runoff, which allows timescale to be expressed as a simple relationship, where

$$T_{T,3} = \frac{V_A}{r_o A_A C}. \tag{21}$$

Equations (19)–(21) can be solved using both morphometric measurements from Table 1 and hydrologic parameters discussed above for a range of D_{84} values. In our models Q_s is constant over time and represents mean sediment discharge during time periods when sediment transport is actively occurring (i.e., wet activity; $Q_s \neq 0$). The three derived sediment transport timescales are presented in Figure 6.

6.3. Results

Timescales for the formation of alluvial fans on Mars depend on grain size as well as the sediment transport relationship method used (see Figure 6). For a range of D_{84} between 10^{-3} and 10^0 m, we show T_T for each of the five alcoves in Table 1 using alcove-specific metrics, where each system corresponds to an individual black line and colored bands enclose each of three models applied. Relationships derived from terrestrial databases include standard deviation from the mean as dashed lines. For Earth-calibrated sediment concentrations, T_T does not depend on grain size and is a constant value (equation (21); orange band in Figure 6). Timescales using cataloged τ^*/τ_c^* values are proportional to $D_{84}^{-2/3}$ and thus display a linear relationship with a negative slope in a logarithmic plot (equation (20); green band in Figure 6). Timescales using a friction law combined with excess sediment transport equations result in a nonlinear relationship where T_T curves display a well-defined global minimum for a unique D_{84} value (equation (19); blue band in Figure 6). For grain sizes $D_{84} < 10^{-2} m$, T_T slowly decreases as grain size increases. However, for $D_{84} > 10^{-1} m$, T_T rapidly increases over 2 orders of magnitude as grain size increases. This is a consequence of the additional D_{84} term in equation (19) when compared to the other two models. When grain size is small, the timescale decreases with grain size, similarly to Method 2. However, as D_{84} approaches a threshold size, the grain size effect on the shear stress (where increased grain size reduces shield stress; equation (17)) becomes the dominant process. As a result τ^* and thus sediment discharge decrease rapidly resulting in larger timescales from $D_{84} \sim 10^{-1}$ m. Note that τ^* can only decrease down to the critical shear stress, since the excess stress

AGU
100
ADVANCING EARTH
AND SPACE SCIENCE

Journal of Geophysical Research: Planets
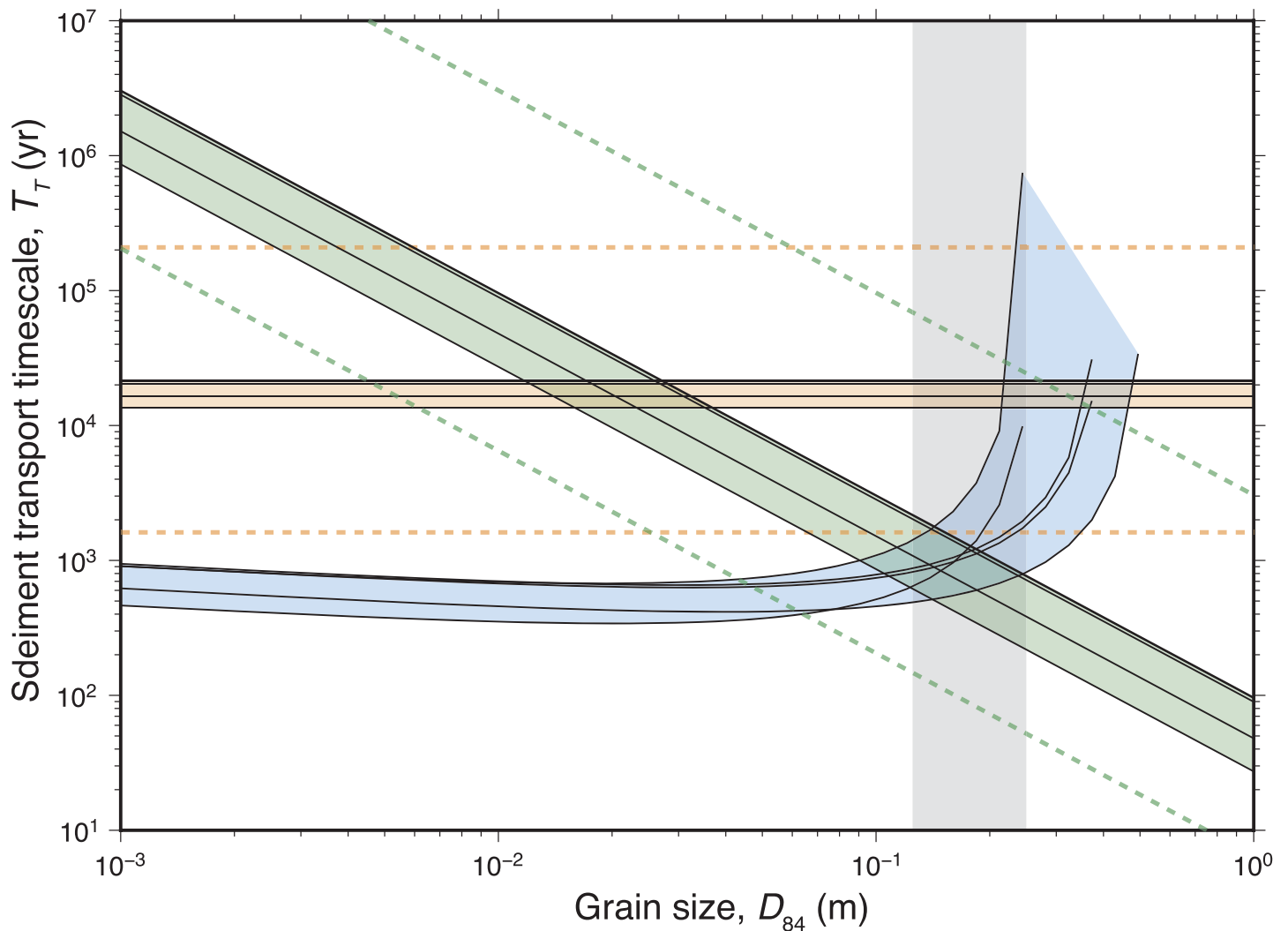
10.1029/2019JE006167

Figure 6. Timescale of sediment transport resulting in alluvial fan deposition as a function of D_{84} (grain size for which 84% of the particles sizes are smaller) for five alcoves in different craters (Roddy, Harris, Holden, Murray, and SE Saheki craters). Blue band = $T_{T,1}$ calculated using the Manning equation, Meyer-Peter and Müller sediment transport equation, and energetic upper limit of runoff from snowmelt from Kite et al. (2013). Green band = $T_{T,2}$ calculated using mean τ_*/τ_{*C} from North American rivers from Pfeiffer et al. (2017) combined with the Meyer-Peter and Müller equation; green dashed lines = $\pm1\sigma$. Orange band = $T_{T,3}$ determined using mean Q_s/Q_w for 411 terrestrial rivers from Dietrich et al. (2017) and energetic upper limit of snowmelt runoff; orange dashed lines = $\pm1\sigma$. Gray box = D_{84} grain sizes estimated from Saheki crater alluvial fan from Morgan et al. (2014; 12.5–25 cm). Note timescales assume zero intermittency (continuous bankfull discharge).

cannot be negative. Consequently, the cutoff in the curves represents the point at which bed shear stress is no longer enough to support sediment transport ($\tau^* < \tau_c^*$; $Q_s = 0$).

The three methods presented differ in their relative tightness and ability to constrain timescales effectively. The methods that make use of the upper limit for runoff from snowmelt can only provide a lower bound on the shortest possible timescales (Methods 1 and 3). Method 2 does not require known water discharge and thus has the tightest constraints on timescale, using only calculated terrestrial ϕ values. Pfeiffer et al. (2017) find that mean ϕ values for quieter tectonic regions are ~1.03, which is equivalent to the lower green dashed line in Figure 6. The gray box in Figure 6 shows estimated grain sizes for an inverted ridge on the alluvial fans in Saheki crater from Morgan et al. (2014). This estimate was obtained from "speckled" textures observed in channel beds from HiRISE imagery (25 cm/pixel), suggesting clasts that are close to or slightly below the resolution limit of the camera ($12.5 < D_{84} < 25$ cm). For these grain sizes we find that formation timescales

for Martian alluvial fans lie broadly between 10^2 and 10^5 years for continuous bankfull flow (i.e., no intermittency). These values can then be compared to and combined with erosional (stream power) timescales in order to better constrain total fluvial activity and how these system may have formed and evolved.

7. Discussion

7.1. Channel Erosion Parameters: Earth Versus Mars

7.1.1. Concavity Index on Mars

Previous work has shown that many channels on Mars display either convex-up or quasi-linear longitudinal profiles with large knickpoints typically thought to reflect the precursor topography of the Martian highlands (Goudge & Fassett, 2018; Irwin et al., 2011). As a result, studies which applied slope-area methods concluded that since $\theta \leq 0$ these systems are either immature and unadjusted to long-lived surface runoff, or sourced from groundwater instead (e.g., Aharonson et al., 2002; Penido et al., 2013; Som et al., 2009). Our results indicate almost all channels incising into crater rims from our database exhibit a slope-area scaling relationship with a mean concavity index of $\theta_\chi = 0.35$. This value is low for typical terrestrial rivers and suggests that average slope decreases with contributing drainage area less than in terrestrial river networks. However, some studies have presented similar concavity indexes on Mars using a variety of methods. For example, Barnhart et al. (2009) used landscape evolution models and found $\theta \sim 0.3$ resulted in the best fit for observed channels in Paraná Valles (for $n = 1$). Stepinski et al. (2004) used fractal descriptors of individual drainage basins to find that $\theta = 0.36$ for Noachian dissected plains. Slope-area plots by Caprarelli and Wang (2012) also found low concavities ~ 0.26; however, Smith (2013) found that large increases in data resolution affect concavity indexes, with a higher-resolution average of $\theta = 0.29$. The occurrence of both concave and convex systems on Mars most likely stems from spatial and temporal variations in erosional processes which depend on groundwater input, initial topography, and the presence of a climate allowing enough geomorphic work to grade (increase the concavity of) channels.

The significance of our calculated concavity index values for crater rims is justified for five reasons: (i) values cluster around a mean value and are not random; (ii) with increasing lengths, channels tend toward the mean concavity index (either due to increased signal:noise or increased adjustment toward global concavity index due to higher fluvial development; see supporting information Figure S5); (iii) concavity index values are higher than what would be expected for acausal topography (e.g., Dodds & Rothman, 2000); (iv) selecting a different section of the same channel (i.e., altering mouth cutoff) has little effect on concavity; and finally, (v) profiles sourced from pristine, undissected crater walls have large concavity indexes $\theta > 1$ (i.e., steep crater walls with little contributing drainage area), which suggest our low mean value is not preconditioned by initial topography. Post-fluvial modification by glacial and aeolian processes is minimal since valleys have preserved their v-shaped cross sections up to the present day. Methods using χ analyses have not been previously applied on Mars, most likely due to the lack of uplift to balance out erosion, which resulted in a transient retreating wall. However, even on Earth achieving steady state is rare (Phillips, 2010). As mentioned in section 3.1, in the case of $U = 0$, any gradient variations in a χ profile will be due to spatial heterogeneity in E or K. On Earth, channel concavity and steepness indexes can be used to infer climatic conditions and/or erosion rates, respectively, and in the absence of uplift and significant lithological contrasts these methods are appropriate for examining climatic controlling processes on Martian crater rim channels.

7.1.2. Implications for Climatic Conditions

In Figure 4, Martian concavity indexes are generally lower than terrestrial (both escarpment and global bedrock channels), whereas steepness indexes are slightly higher than quiescent terrestrial channels. Although Martian parameter values have a large spread when compared to distinct terrestrial escarpment basins sourced from the same location, their spread is much less than the global terrestrial values which span a range of tectonic, lithological, and climatic settings. Conceptually, climate affects profile concavity index by changing the hydrology and sediment production of a watershed (Whipple & Tucker, 1999). On Earth, low concavity indexes are characteristic of semiarid to arid environments, whereas higher values ~ 0.7 would be typical of a humid environment (Bull, 2002; Barnhart et al., 2009). For example, in tectonically stable settings, Zaprowski et al. (2005) found that greater mean annual precipitation lead to more concave profiles. Further, a global assessment of terrestrial channels found that normalized concavity index of rivers decreased with increasing aridity (Chen et al., 2019). These observations may be a result of nonlinearity between discharge and drainage area, which is used as a proxy for discharge in equation (1). Nonlinear relationships between the two are particularly pronounced in dry climates, where rainstorms tend to be
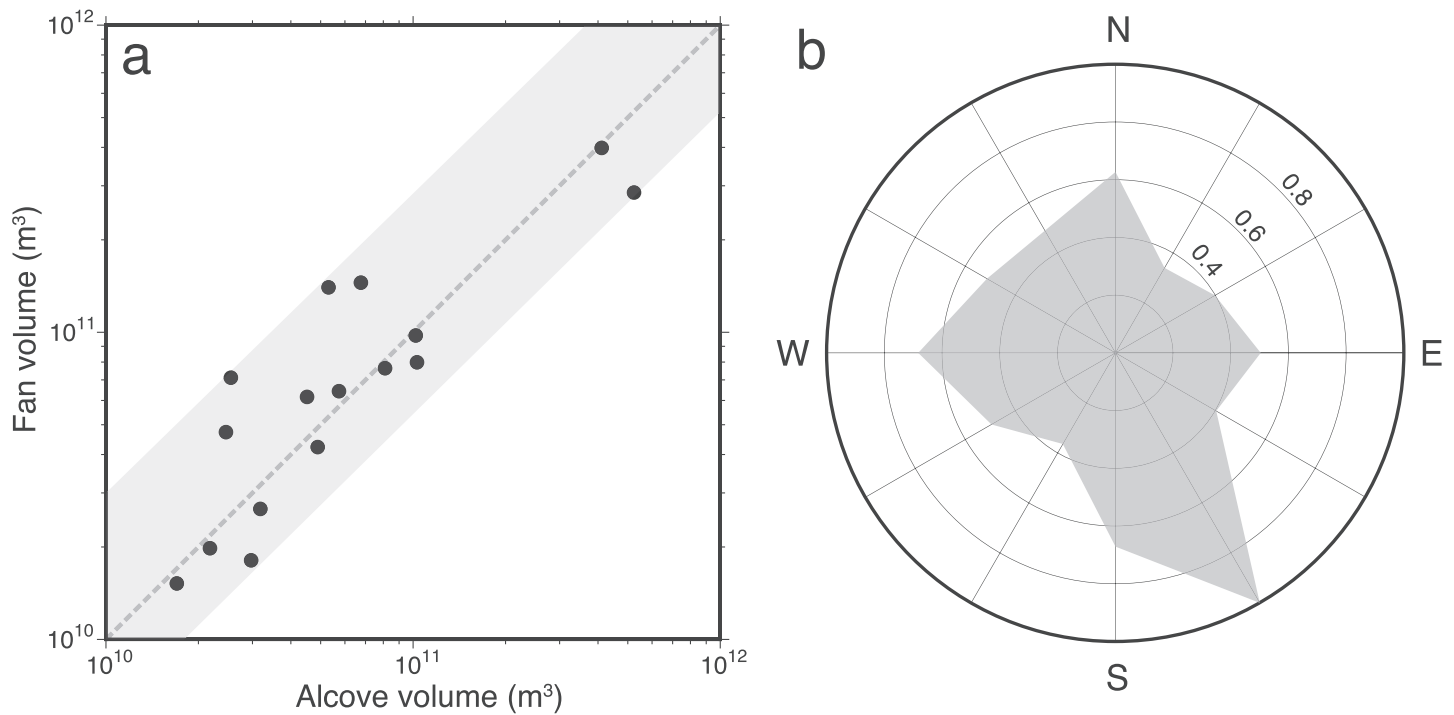
Figure 7. (a) Estimated volumes of eroded alcoves and fan deposits; gray dashed line = 1-to-1 line. Gray band = total deviation of values from 1-to-1 line (see supporting information Table S1). (b) Orientation of 216 crater rim channels lengths normalized to 1.

short-lived (resulting in in-stream losses) and spatially heterogenous within the drainage basin (Chen et al., 2019; Sólyom & Tucker, 2004).

Similarly, steepness index values also show a dependence on aridity (e.g., Harel et al., 2016). For example, scarp evolution models using 2-D advective and diffusive processes by Kooi and Beaumont (1994) showed that for a relatively arid climate, steep escarpments are predicted, while for relatively humid, temperate climatic conditions only major escarpments preserve a somewhat significant gradient. Similarly, a global analysis of channel steepness index found that the highest values on Earth were found in the Atacama Desert and Namibia (Hilley et al., 2019). Kooi and Beaumont (1994) suggest that this may be because increasing aridity will decrease weathering more than it decreases fluvial transport. Consequently, diffusive processes become less important and advective processes dominate, resulting in the development of a steeper, more angular landscape.

The Western Ghats experience annual precipitation rates exceeding 6,000 mm/year at the scarp (Gunnell, 1997). Serra Geral, although humid, has lower annual precipitation rates of <2,500 mm/year and those in the western Great Escarpment in South Africa do not reach 1,000 mm/year (Alvares et al., 2013; Dintwe et al., 2015; Hijmans et al., 2005). In Figure 4, Mars channels are most dissimilar to the Western Ghats (high θ_χ, low $k_{s,\chi}$; extremely humid) and very similar to the South African escarpment (low θ_χ, high $k_{s,\chi}$; semiarid), which would support an arid environment for Martian channels under a quiescent setting. This is consistent with the absence of exit breaches from water accumulation in craters with alluvial fans when compared to older (Noachian) paleolakes (Goudge et al., 2016). The surprising nondetection of Martian fluvial parameters' dependence on latitude, elevation, or orientation can be explained by climatic settings and fluvial processes which were broadly consistent across the systems globally, and likely occurred over similar timescales.

7.2. Fluvial Timescales, Rates, and Intermittency

The derived timescales required to form the erosional alcove and depositional fans using two techniques vary over multiple orders of magnitude and are primarily dependent on unknown rock properties on Mars (i.e., erodability and grain size). The closed sediment loop is evident from similar volumes obtained from eroded and deposited sediment in Figure 7a. Erosional timescales in Figure 5 suggest that channels could not have been incising for longer than 1 Gyr for even the lowest erodabilities. Surface materials in the crater rims

likely consist of basalts, which would suggest very low erodabilities characteristic of granitic/metamorphic rocks are unlikely. This provides us with a conservative upper limit on cumulative years with nonzero runoff (10^8 years) since this value incorporates a terrestrial intermittency into the erodability. Sediment transport timescales in Figure 6 provide a conservative lower bound of 10^2 years and a liberal upper bound of 10^6 years for grain sizes observed in Saheki crater. This method provides tighter constraints on wet activity due to the narrow range of grain sizes estimated by Morgan et al. (2014) compared to the full range of possible erodability values, which are challenging to accurately estimate even on Earth. In addition, sediment transport results assume zero intermittency and thus correlate only with wet activity. Consequently, we focus on sediment transport timescales and find that crater rim channels on Mars likely did not erode for less than 100 years or longer than 1 Myr, precluding catastrophic fluvial events resulting from impacts or individual volcanic eruptions.

Although this range provides useful limits on total amount of time fluvial processes were active, they do not constrain important details on the intermittency of fluvial conditions, in particular the frequency or length of time periods for which water did not flow during the generation and evolution of these systems (Kite, 2019). If conditions were arid, fluvial episodes could have been rare and these systems may have experienced many years of inactivity interspersed with shorter bursts of fluvial erosion. Terrestrial studies have previously incorporated climate variability and stochasticity into derivations of E and Q_w by integrating hydrology, rainfall intensity and frequency, evapotranspiration rates, soil moisture, and sediment flux, among others (see, e.g., Deal et al., 2018; Gasparini et al., 2007; Lague, 2014; Scherler et al., 2017; Tucker & Bras, 2000; Whittaker, 2012). However, we note that our intermittency is likely a consequence of periodical insolation resulting in snowmelt (see section 7.3). Our sediment transport models estimate time-averaged values for wet periods with a constant Q_w (> 0) when insolation occurs, and improved models of melting or obliquity cyclicity on Mars may inform more realistic distributions of $Q_w(t)$.

To estimate the intermittency frequency of our fan systems (=wet years/total years between initiation and cessation of fan buildup), we use results from Kite et al. (2017) where aggradation times for alluvial fans on Mars were estimated using records of embedded craters within deposits. Their results suggest a lower bound for total exposure time of fan buildup ∼20 Myr. Using these values, the highest intermittency frequency for our channels would be 5% and the lowest would be 0.0005% (for 1-Myr and 100-year wet activity, respectively). If we take the intersection of the two most well-constrained curves in Figure 6, which lies within the range of observed grain sizes, we obtain a formation time of 2×10^3 years, and an average intermittency frequency of 0.01%. This coincides with ∼2 hr of wet activity per Martian year, consistent with arid environments on Earth (Woodyer, 1968). The lowest intermittency frequencies would suggest similar total wet activity in a decade, which is still observed in extremely arid environments on Earth, indicating that even the shortest flow timescales on Mars are within observed terrestrial ranges, where channel morphology can be set by hours-long storms in decadal timeframes (Buhler et al., 2014).

We can assess this fluvial intermittency by comparing denudation rates as a function of erosional timescales for bedrock rivers on Earth. Sadler and Jerolmack (2014) showed that for longer averaging times ($>10^7$ years) linear bedrock denudation rates on Earth approach 10^{-2} mm/year and for shorter times (<1 year) typical denudation values increase to $>10^4$ mm/year (see Figure 8). Using our calculated mean denudation, $\bar{z}_A = 260$ m, we find that denudation rates range between ∼10^3 to ∼10^{-1} mm/year. For the longer 20-Ma timescale lower limit from fan buildup, denudation rates are 10^{-2} mm/year. Figure 8 illustrates how observed erosion rates and intermittencies observed on Mars (in this study and from previous work) are consistent with the established relationship between erosion rates and averaged time, which we observe on Earth (Gallen et al., 2015; Golombek et al., 2014; Sadler & Jerolmack, 2014).

7.3. Orientation and Sources

The intermittent behavior of Martian channels requires a source that is both recurring and long-lived over millions of years. Observed dendritic patterns, strong slope-area relations, and initiation at highly elevated ridges suggest channels are probably sourced from precipitation, either in the form of rain or snow (Moore & Howard, 2005). Drainage basin boundaries coincide with crater rim scarp tops, and there is minimal evidence for fluvial incision on plateaus beyond the crater walls. A distribution of channel orientations is shown in Figure 7b, which shows a predominance of SE directions. Previous works demonstrated that alluvial fan volumes have similar distributions with N-S predominance (Grant & Wilson, 2012; Morgan et al., 2018). It has been suggested that the source of water required to carve these channels may have been snowmelt
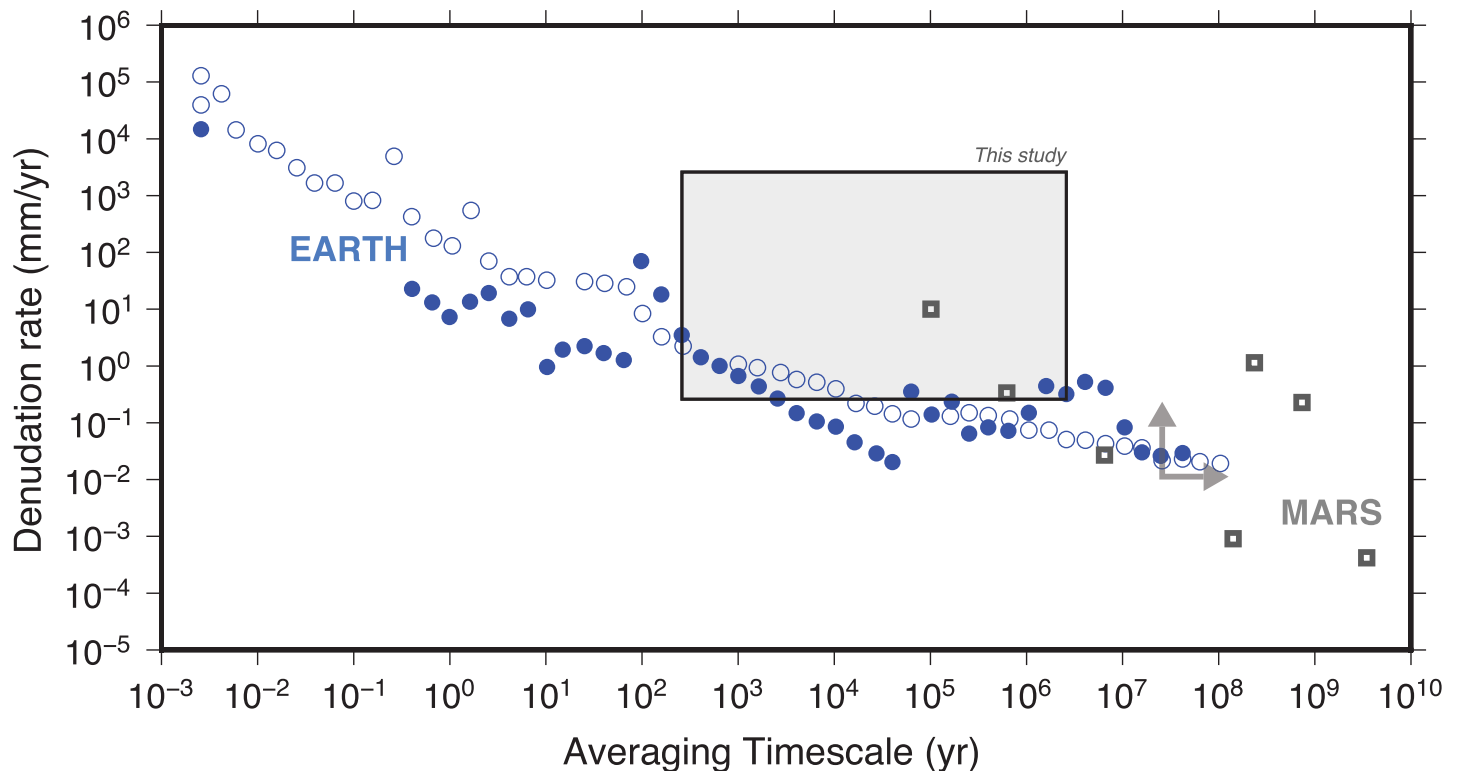
Figure 8. Linear bedrock erosion rates as a function of averaging time on Earth and Mars. Black box = range of values for Martian global crater rim channels sourcing alluvial fans in this study. Blue circles = average bedrock erosion rates in terrestrial rivers from Sadler and Jerolmack (2014). Open blue circles = accumulation rates on terrestrial alluvial plains from Sadler and Jerolmack (2014). Gray bounding arrows = minimum Martian alluvial fan buildup from Kite et al. (2017). Gray squares = previous averages for crater degradation, alluvial fan, and lightly cratered layered terrain erosion rates on Mars (Golombek et al., 2014, and references therein).

released after annual or epochal accumulation of snow in the headwater source on interior crater rims (Morgan et al., 2018). For example, during periods of high orbital obliquity, increased polar summer insolation enhances polar ice sublimation, increasing both atmospheric water content and circulation, leading to a more intense water cycle (Forget et al., 2006; Madeleine et al., 2009; 2014). Precipitation of snow becomes widespread in the midlatitudes and snow could accumulate in favorable locations such as crater walls where it sourced snowmelt (de Haas, 2016; Williams & Irwin, 2009). In between these periods of high obliquity, large periods of inactivity could explain the intermittency of alcove formation.

On Earth, steep regional slopes and mountain ranges act as potential barriers that moist wind systems have to surpass. For example, the Western Ghats act as a 1,500-km-long windward barrier, which are the first highlands that the southwest monsoon winds encounter while traveling along coastal plains (Gunnell, 1997). The dumping of rain or snow on prevailing windward slopes occurs even in dry climates (Barnhart et al., 2009). On Mars, steep crater walls result in significant relief at the kilometer scale in otherwise flat plateaus. The locations of large alluvial fans in our database are spread over a wide range of longitudes but constrained over midlatitudes. Further, Figure 7b shows a stronger predominance of SE channel directions. Similarly to obliquity-dependent snowmelt, channel generation from hypothetical orographic winds depositing snow on crater walls could explain preferred orientations, latitudinal clustering, and concentrated precipitation on rims.

8. Conclusion

We assessed the geomorphology and topography of a global database of >200 channels in crater walls, which source alluvial fans on Mars (Late Hesperian - Amazonian age). Because both the sediment sources (eroded valleys) and the adjacent fans are well preserved, we derived fluvial activity timescales for these systems using both detachment- and transport-limited models on bedrock channels and deposited sediments, respectively. Results indicate that channels must have been actively flowing for 10^2–10^6 years assuming continuous

flow (no intermittency). Better constraints require improved understanding of variables such as grain size and rock erodability. When combined with previously estimated buildup ages for these systems (>20 Ma), flow intermittency frequencies fall within highly arid ranges on Earth, with yearly to decadal hour-long flows with channel-forming discharges. Key fluvial geometry parameters derived from stream power law suggest mapped channels are not immature and support a precipitation source in an arid climate setting. The confined spatial distribution of these systems, both regionally and locally within craters, suggests an origin from snowmelt due to either obliquity variations or orographic accumulation. These results support a long-lived time span of wet activity, which allowed these spatially distributed fluvial systems to evolve recurrently under broadly similar conditions at a global scale.

References

Aharonson, O., Zuber, M. T., Rothman, D. H., Schorghofer, N., & Whipple, K. X. (2002). Drainage basins and channel incision on Mars. *Proceedings of the National Academy of Sciences*, *99*(4), 1780–1783.

Alvares, C. A., Stape, J. L., Sentelhas, P. C., de Moraes, G., Leonardo, J., & Sparovek, G. (2013). Köppen's climate classification map for Brazil. *Meteorologische Zeitschrift*, *22*(6), 711–728.

Barnhart, C. J., Howard, A. D., & Moore, J. M. (2009). Long-term precipitation and late-stage valley network formation: Landform simulations of Parana Basin, Mars. *Journal of Geophysical Research*, *114*, E01003. https://doi.org/10.1029/2008JE003122

Beyer, R. A., Alexandrov, O., & McMichael, S. (2018). The Ames Stereo Pipeline: NASA's open source software for deriving and processing terrain data. *Earth and Space Science*, *5*(9), 537–548.

Blair, T. C., & McPherson, J. G. (1994). Alluvial fans and their natural distinction from rivers based on morphology, hydraulic processes, sedimentary processes, and facies assemblages. *Journal of Sedimentary Research*, *64*(3a), 450–489.

Bouquety, A., Sejourné, A., Costard, F., Mercier, D., & Bouley, S. (2019). Morphometric evidence of 3.6 Ga glacial valleys and glacial cirques in martian highlands, South of Terra Sabaea. *Geomorphology*, *334*, 91–111.

Braun, J. (2018). A review of numerical modeling studies of passive margin escarpments leading to a new analytical expression for the rate of escarpment migration velocity. *Gondwana Research*, *53*, 209–224.

Braun, J., & Beaumont, C. (1989). A physical explanation of the relation between flank uplifts and the breakup unconformity at rifted continental margins. *Geology*, *17*(8), 760–764.

Buffington, J. M., & Montgomery, D. R. (1997). A systematic analysis of eight decades of incipient motion studies, with special reference to gravel-bedded rivers. *Water Resources Research*, *33*, 1993–2029. https://doi.org/10.1029/96WR03190

Buhler, P. B., Fassett, C. I., Head, IIIJ. W., & Lamb, M. P. (2014). Timescales of fluvial activity and intermittency in Milna Crater, Mars. *Icarus*, *241*, 130–147.

Bull, L. J. (2002). *Dryland rivers: Hydrology and geomorphology of semi-arid channels*. Chichester, UK: John Wiley.

Campforts, B., & Govers, G. (2015). Keeping the edge: A numerical method that avoids knickpoint smearing when solving the stream power law. *Journal of Geophysical Research: Earth Surface*, *120*, 1189–1205. https://doi.org/10.1002/2014JF003376

Caprarelli, G., & Wang, B. (2012). Wet Mars implications of revised scaling calculations for Evros Vallis. *Australian Journal of Earth Sciences*, *59*(2), 263–276.

Chen, S.-A., Michaelides, K., Grieve, S. W., & Singer, M. B. (2019). Aridity is expressed in river topography globally. *Nature*, *573*, 573–577.

Coleman, N. M. (2015). Hydrographs of a Martian flood from the breach of Galilaei Crater. *Geomorphology*, *236*, 90–108.

Conway, S. J., Balme, M. R., Murray, J. B., Towner, M. C., Okubo, C. H., & Grindrod, P. M. (2011). The indication of Martian gully formation processes by slope–area analysis. *Geological Society, London, Special publications*, *356*(1), 171–201.

Czarnota, K., Roberts, G., White, N., & Fishwick, S. (2014). Spatial and temporal patterns of Australian dynamic topography from river profile modeling. *Journal of Geophysical Research: Solid Earth*, *119*, 1384–1424. https://doi.org/10.1002/2013JB010436

de Haas, T., Kleinhans, M., de Jong, S., & Hauber, E. (2016). Life, death and revival of debris-flow fans on Earth and Mars: Fan dynamics and climatic inferences (Ph.D. thesis), University Utrecht.

Deal, E., Braun, J., & Botter, G. (2018). Understanding the role of rainfall and hydrology in determining fluvial erosion efficiency. *Journal of Geophysical Research: Earth Surface*, *123*, 744–778. https://doi.org/10.1002/2017JF004393

DiBiase, R. A., & Whipple, K. X. (2011). The influence of erosion thresholds and runoff variability on the relationships among topography, climate, and erosion rate. *Journal of Geophysical Research*, *116*, F04036. https://doi.org/10.1029/2011JF002095

Dietrich, W. E., Palucis, M. C., Williams, R. M., Lewis, K. W., Rivera-Hernandez, F., & Sumner, D. Y. (2017). Fluvial Gravels on Mars. In D. Tsutsumi & J. B. Laronne (Eds.), *Gravel-Bed Rivers*. https://doi.org/10.1002/9781118971437.ch28

Dintwe, K., Okin, G. S., D'Odorico, P., Hrast, T., Mladenov, N., Handorean, A., et al. (2015). Soil organic C and total N pools in the Kalahari: Potential impacts of climate change on C sequestration in savannas. *Plant and soil*, *396*(1-2), 27–44.

Dodds, P. S., & Rothman, D. H. (2000). Scaling, universality, and geomorphology. *Annual Review of Earth and Planetary Sciences*, *28*(1), 571–610.

Egholm, D. L., Knudsen, M. F., & Sandiford, M. (2011). Lifespan of mountain ranges scaled by feedbacks between landsliding and erosion by rivers. *Nature Letters*, *498*, 475–477.

Ferrier, K. L., Huppert, K. L., & Perron, J. T. (2013). Climatic control of bedrock river incision. *Nature*, *496*(7444), 206.

Forget, F., Haberle, R., Montmessin, F., Levrard, B., & Head, J. (2006). Formation of glaciers on Mars by atmospheric precipitation at high obliquity. *Science*, *311*(5759), 368–371.

Gallen, S. F. (2018). Lithologic controls on landscape dynamics and aquatic species evolution in post-orogenic mountains. *Earth and Planetary Science Letters*, *493*, 150–160.

Gallen, S. F., Pazzaglia, F. J., Wegmann, K. W., Pederson, J. L., & Gardner, T. W. (2015). The dynamic reference frame of rivers and apparent transience in incision rates. *Geology*, *43*(7), 623–626.

Gasparini, N. M., Whipple, K. X., & Bras, R. L. (2007). Predictions of steady state and transient landscape morphology using sediment-flux-dependent river incision models. *Journal of Geophysical Research*, *112*, F03S09. https://doi.org/10.1029/2006JF000567

Golombek, M., Warner, N., Ganti, V., Lamb, M., Parker, T., Fergason, R. L., & Sullivan, R. (2014). Small crater modification on Meridiani Planum and implications for erosion rates and climate change on Mars. *Journal of Geophysical Research: Planets*, *119*, 2522–2547. https://doi.org/10.1002/2014JE004658

Goren, L. (2016). A theoretical model for fluvial channel response time during time-dependent climatic and tectonic forcing and its inverse applications. *Geophysical Research Letters*, *43*, 10–753. https://doi.org/10.1002/2016GL070451

Goudge, T. A., & Fassett, C. I. (2018). Incision of Licus Vallis, Mars, from multiple lake overflow floods. *Journal of Geophysical Research: Planets*, *123*, 405–420. https://doi.org/10.1002/2017JE005438

Goudge, T. A., Fassett, C. I., Head, J. W., Mustard, J. F., & Aureli, K. L. (2016). Insights into surface runoff on early Mars from paleolake basin morphology and stratigraphy. *Geology*, *44*(6), 419–422.

Grant, J. A., & Wilson, S. A. (2012). A possible synoptic source of water for alluvial fan formation in southern Margaritifer Terra, Mars. *Planetary and Space Science*, *72*(1), 44–52.

Gunnell, Y. (1997). Relief and climate in South Asia: The influence of the Western Ghats on the current climate pattern of peninsular India. *International Journal of Climatology*, *17*(11), 1169–1182.

Hack, J. T. (1957). *Studies of longitudinal stream profiles in Virginia and Maryland* (Vol. 294). Berkeley, CA: US Government Printing Office.

Harel, M.-A., Mudd, S., & Attal, M. (2016). Global analysis of the stream power law parameters based on worldwide 10Be denudation rates. *Geomorphology*, *268*, 184–196.

Hayden, A. T., Lamb, M. P., Fischer, W. W., Ewing, R. C., McElroy, B. J., & Williams, R. M. (2019). Formation of sinuous ridges by inversion of river-channel belts in Utah, USA, with implications for Mars. *Icarus*, *332*, 92–110.

Hijmans, R. J., Cameron, S. E., Parra, J. L., Jones, P. G., & Jarvis, A. (2005). Very high resolution interpolated climate surfaces for global land areas. *International journal of climatology*, *25*(15), 1965–1978.

Hilley, G. E., Porder, S., Aron, F., Baden, C. W., Johnstone, S. A., Liu, F., et al. (2019). Earth's topographic relief potentially limited by an upper bound on channel steepness. *Nature Geoscience*, *12*, 828–832.

Hoke, M. R., Hynek, B. M., & Tucker, G. E. (2011). Formation timescales of large Martian valley networks. *Earth and Planetary Science Letters*, *312*(1-2), 1–12.

Howard, A. D. (1994). A detachment-limited model of drainage basin evolution. *Water resources research*, *30*, 2261–2285. https://doi.org/10.1029/94WR00757

Howard, A. D., Breton, S., & Moore, J. M. (2016). Formation of gravel pavements during fluvial erosion as an explanation for persistence of ancient cratered terrain on Titan and Mars. *Icarus*, *270*, 100–113.

Howard, A. D., & Kerby, G. (1983). Channel changes in badlands. *Geological Society of America Bulletin*, *94*(6), 739–752.

Irwin, R. P., Craddock, R. A., Howard, A. D., & Flemming, H. L. (2011). Topographic influences on development of Martian valley networks. *Journal of Geophysical Research*, *116*, E02005. https://doi.org/10.1029/2010JE003620

Kite, E. S. (2019). Geologic constraints on early Mars climate. *Space Science Reviews*, *215*(1), 10.

Kite, E. S., Halevy, I., Kahre, M. A., Wolff, M. J., & Manga, M. (2013). Seasonal melting and the formation of sedimentary rocks on Mars, with predictions for the Gale Crater mound. *Icarus*, *223*(1), 181–210.

Kite, E. S., Mayer, D. P., Wilson, S. A., Davis, J. M., Lucas, A. S., & Stucky de Quay, G. (2019). Persistence of intense, climate-driven runoff late in Mars history. *Science Advances*, *5*(3), eaav7710.

Kite, E. S., Sneed, J., Mayer, D. P., & Wilson, S. A. (2017). Persistent or repeated surface habitability on Mars during the late Hesperian-Amazonian. *Geophysical Research Letters*, *44*, 3991–3999. https://doi.org/10.1002/2017GL072660

Kleinhans, M. G. (2005). Flow discharge and sediment transport models for estimating a minimum timescale of hydrological activity and channel and delta formation on Mars. *Journal of Geophysical Research*, *110*, E12003. https://doi.org/10.1029/2005JE00252

Kooi, H., & Beaumont, C. (1994). Escarpment evolution on high-elevation rifted margins: Insights derived from a surface processes model that combines diffusion, advection, and reaction. *Journal of Geophysical Research*, *99*, 12,191–12,209. https://doi.org/10.1029/94JB00047

Kraal, E. R., Asphaug, E., Moore, J. M., Howard, A., & Bredt, A. (2008). Catalogue of large alluvial fans in Martian impact craters. *Icarus*, *194*(1), 101–110.

Lague, D. (2014). The stream power river incision model: Evidence, theory and beyond. *Earth Surface Processes and Landforms*, *39*(1), 38–61.

Lamb, M. P., Dietrich, W. E., & Sklar, L. S. (2008). A model for fluvial bedrock incision by impacting suspended and bed load sediment. *Journal of Geophysical Research*, *113*, F03025. https://doi.org/10.1029/2007JF000915

Madeleine, J.-B., Forget, F., Head, J. W., Levrard, B., Montmessin, F., & Millour, E. (2009). Amazonian northern mid-latitude glaciation on Mars: A proposed climate scenario. *Icarus*, *203*(2), 390–405.

Madeleine, J.-B., Head, J. W., Forget, F., Navarro, T., Millour, E., Spiga, A., et al. (2014). Recent ice ages on Mars: The role of radiatively active clouds and cloud microphysics. *Geophysical Research Letters*, *41*, 4873–4879. https://doi.org/10.10002/2014GL059861

Malin, M. C., Bell, J. F., Cantor, B. A., Caplinger, M. A., Calvin, W. M., Clancy, R. T., et al. (2007). Context camera investigation on board the Mars Reconnaissance Orbiter. *Journal of Geophysical Research*, *112*, E05S04. https://doi.org/10.1029/2006JE002808

Matmon, A., Bierman, P., & Enzel, Y. (2002). Pattern and tempo of great escarpment erosion. *Geology*, *30*(12), 1135–1138.

Mayer, D., & Kite, E. (2016). An integrated workflow for producing digital terrain models of Mars from CTX and HiRISE stereo data using the NASA Ames Stereo Pipeline. *Lunar and Planetary Science Conference*, 47, 1241.

McGovern, P. J., Solomon, S. C., Smith, D. E., Zuber, M. T., Simons, M., Wieczorek, M. A., et al. (2002). Localized gravity/topography admittance and correlation spectra on Mars: Implications for regional and global evolution. *Journal of Geophysical Research*, *107*(E12), 19–1. https://doi.org/10.1029/2002JE001854

Meyer-Peter, E., & Müller, R. (1948). Formulas for bed-load transport, *IAHSR 2nd meeting*. Stockholm.

Moore, J. M., & Howard, A. D. (2005). Large alluvial fans on Mars. *Journal of Geophysical Research*, *110*, E04005. https://doi.org/10.1029/2004JE002352

Morgan, A., Howard, A., Hobley, D. E., Moore, J. M., Dietrich, W. E., Williams, R. M., et al. (2014). Sedimentology and climatic environment of alluvial fans in the Martian Saheki crater and a comparison with terrestrial fans in the Atacama Desert. *Icarus*, *229*, 131–156.

Morgan, A., Wilson, S., Howard, A., Craddock, R., & Grant, J. (2018). Global distribution of alluvial fans and deltas on Mars. In *Lunar and Planetary Science Conference* (Vol. 49). Houston, TX.

Murphy, B. P., Johnson, J. P., Gasparini, N. M., & Sklar, L. S. (2016). Chemical weathering as a mechanism for the climatic control of bedrock river incision. *Nature*, *532*(7598), 223.

Ollier, C. (1985). Morphotectonics of continental margins with great escarpments. *Tectonic geomorphology*, *15*, 3–25.

Palucis, M. C., Dietrich, W. E., Hayes, A. G., Williams, R. M., Gupta, S., Mangold, N., et al. (2014). The origin and evolution of the Peace Vallis fan system that drains to the Curiosity landing area, Gale Crater, Mars. *Journal of Geophysical Research*, *119*, 705–728. https://doi.org/10.1002/2013JE004583

Parker, G. (1991). Selective sorting and abrasion of river gravel. II: Applications. *Journal of Hydraulic Engineering*, *117*(2), 150–171.

Paul, J. D., Roberts, G. G., & White, N. (2014). The African landscape through space and time. *Tectonics*, *33*, 898–935. https://doi.org/10.1002/2013TC003479

Penido, J. C., Fassett, C. I., & Som, S. M. (2013). Scaling relationships and concavity of small valley networks on Mars. *Planetary and Space Science*, *75*, 105–116.

Perron, J. T. (2017). Climate and the pace of erosional landscape evolution. *Annual Review of Earth and Planetary Sciences*, *45*, 561–591.

Perron, J. T., & Royden, L. (2013). An integral approach to bedrock river profile analysis. *Earth Surface Processes and Landforms*, *38*(6), 570–576.

Peters, G., Carey, E., Anderson, R., Abbey, W., Kinnett, R., Watkins, J., et al. (2018). Uniaxial compressive strengths of rocks drilled at Gale Crater, Mars. *Geophysical Research Letters*, *45*, 108–116. https://doi.org/10.1002/2017GL075965

Pfeiffer, A. M., Finnegan, N. J., & Willenbring, J. K. (2017). Sediment supply controls equilibrium channel geometry in gravel rivers. *Proceedings of the National Academy of Sciences*, *114*(13), 3346–3351.

Phillips, J. D. (2010). The job of the river. *Earth Surface Processes and Landforms: The Journal of the British Geomorphological Research Group*, *35*(3), 305–313.

Recking, A. (2012). Simple method for calculating reach-averaged bed-load transport. *Journal of Hydraulic Engineering*, *139*(1), 70–75.

Roberts, G., White, N., Martin-Brandis, G., & Crosby, A. (2012). An uplift history of the Colorado Plateau and its surroundings from inverse modeling of longitudinal river profiles. *Tectonics*, *31*, TC4022. https://doi.org/10.1029/2012TC003107

Roe, G. H., Montgomery, D. R., & Hallet, B. (2002). Effects of orographic precipitation variations on the concavity of steady-state river profiles. *Geology*, *30*(2), 143–146.

Rosenbloom, N. A., & Anderson, R. S. (1994). Hillslope and channel evolution in a marine terraced landscape, Santa Cruz, California. *Journal of Geophysical Research*, *99*, 14,013–14,029.

Royden, L., & Perron, J. T. (2013). Solutions of the stream power equation and application to the evolution of river longitudinal profiles. *Journal of Geophysical Research: Earth Surface*, *118*, 497–518. https://doi.org/10.1002/jgrf.20031

Rudge, J. F., Roberts, G. G., White, N. J., & Richardson, C. N. (2015). Uplift histories of Africa and Australia from linear inverse modeling of drainage inventories. *Journal of Geophysical Research: Earth Surface*, *120*, 894–914. https://doi.org/10.1002/2014JF003297

Ruiz, J. (2014). The early heat loss evolution of Mars and their implications for internal and environmental history. *Scientific reports*, *4*, 4338.

Sadler, P. M., & Jerolmack, D. J. (2014). Scaling laws for aggradation, denudation and progradation rates: The case for time-scale invariance at sediment sources and sinks. *Geological Society, London, Special Publications*, *404*, SP404–7.

Scherler, D., DiBiase, R. A., Fisher, G. B., & Avouac, J.-P. (2017). Testing monsoonal controls on bedrock river incision in the Himalaya and Eastern Tibet with a stochastic-threshold stream power model. *Journal of Geophysical Research: Earth Surface*, *122*, 1389–1429. https://doi.org/10.1002/2016JF004011

Schoenbohm, L., Whipple, K., Burchfiel, B., & Chen, L. (2004). Geomorphic constraints on surface uplift, exhumation, and plateau growth in the Red River region, Yunnan Province, China. *Geological Society of America Bulletin*, *116*(7-8), 895–909.

Sinha, S. K., & Parker, G. (1996). Causes of concavity in longitudinal profiles of rivers. *Water Resources Research*, *32*, 1417–1428. https://doi.org/10.1029/95WR03819

Sklar, L., & Dietrich, W. E. (1998). River longitudinal profiles and bedrock incision models: Stream power and the influence of sediment supply. *American Geophysical Union (AGU)*, *107*, 237–260. https://doi.org/10.1029/GM107p0237

Sklar, L. S., & Dietrich, W. E. (2001). Sediment and rock strength controls on river incision into bedrock. *Geology*, *29*(12), 1087–1090.

Smith, P. (2013). The effect of resolution on scaling relations and concavity on valley networks on Mars. *Papers in Resource Analysis*, *144*, 15.

Sólyom, P. B., & Tucker, G. E. (2004). Effect of limited storm duration on landscape evolution, drainage basin geometry, and hydrograph shapes. *Journal of Geophysical Research*, *109*, F03012. https://doi.org/10.1029/2003JF000032

Som, S. M., Montgomery, D. R., & Greenberg, H. M. (2009). Scaling relations for large Martian valleys. *Journal of Geophysical Research*, *114*, E02005. https://doi.org/10.1029/2008JE003132

Stepinski, T., Collier, M., McGovern, P., & Clifford, S. (2004). Martian geomorphology from fractal analysis of drainage networks. *Journal of Geophysical Research*, *109*, E02005. https://doi.org/10.1029/2003JE002098

Stock, J. D., & Montgomery, D. R. (1999). Geologic constraints on bedrock river incision using the stream power law. *Journal of Geophysical Research*, *104*, 4983–4993.

Stucky de Quay, G., Roberts, G. G., Rood, D. H., & Fernandes, V. M. (2019). Holocene uplift and rapid fluvial erosion of Iceland: A record of post-glacial landscape evolution. *Earth and Planetary Science Letters*, *505*, 118–130.

Thomson, B., Bridges, N., Cohen, J., Hurowitz, J., Lennon, A., Paulsen, G., & Zacny, K. (2013). Estimating rock compressive strength from Rock Abrasion Tool (RAT) grinds. *Journal of Geophysical Research: Planets*, *118*, 1233–1244. https://doi.org/10.1002/jgre.20061

Tucker, G. E., & Bras, R. L. (2000). A stochastic approach to modeling the role of rainfall variability in drainage basin evolution. *Water Resources Research*, *36*, 1953–1964. https://doi.org/10.1029/2000WR900065

Tucker, G. E., & Slingerland, R. L. (1994). Erosional dynamics, flexural isostasy, and long-lived escarpments: A numerical modeling study. *Journal of Geophysical Research*, *99*, 12,229–12,243.

Tucker, G., & Whipple, K. (2002). Topographic outcomes predicted by stream erosion models: Sensitivity analysis and intermodel comparison. *Journal of Geophysical Research*, *107*(B9), ETG 1–1-ETG 1-16. https://doi.org/10.1029/2001JB000162

van der Beek, P., Summerfield, M. A., Braun, J., Brown, R. W., & Fleming, A. (2002). Modeling postbreakup landscape development and denudational history across the southeast African (Drakensberg Escarpment) margin. *Journal of Geophysical Research*, *107*(B12), 2351. https://doi.org/10.1029/2001JB000744

Whipple, K. X., Hancock, G. S., & Anderson, R. S. (2000). River incision into bedrock: Mechanics and relative efficacy of plucking, abrasion, and cavitation. *Geological Society of America Bulletin*, *112*(3), 490–503.

Whipple, K. X., Kirby, E., & Brocklehurst, S. H. (1999). Geomorphic limits to climate-induced increases in topographic relief. *Nature*, *401*(6748), 39.

Whipple, K. X., & Tucker, G. E. (1999). Dynamics of the stream-power river incision model: Implications for height limits of mountain ranges, landscape response timescales, and research needs. *Journal of Geophysical Research*, *104*, 17,661–17,674.

Whittaker, A. C. (2012). How do landscapes record tectonics and climate? *Lithosphere*, *4*(2), 160–164.

Williams, R. M., Chidsey Jr, T. C., & Eby, D. E. (2007). Exhumed paleochannels in central Utah-Analogs for raised curvilinear features on Mars. *Utah Geological Association*, *36*, 221–235.

Williams, R., & Irwin, R. (2009). Morphology of lava-capped inverted valleys near St George, Utah: Analogs for Martian sinuous ridges. In *Lunar and Planetary Science Conference*, *40*. Houston, TX.

Wobus, C., Whipple, K. X., Kirby, E., Snyder, N., Johnson, J., Spyropolou, K., et al. (2006). Tectonics from topography: Procedures, promise, and pitfalls. *Special Papers-Geological Society of America*, *398*, 55.

Woodyer, K. (1968). Bankfull frequency in rivers. *Journal of Hydrology*, *6*(2), 114–142.

Zaprowski, B. J., Pazzaglia, F. J., & Evenson, E. B. (2005). Climatic influences on profile concavity and river incision. *Journal of Geophysical Research*, *110*, F03004. https://doi.org/10.1029/2004JF000138

Zimmer, P. D., & Gabet, E. J. (2018). Assessing glacial modification of bedrock valleys using a novel approach. *Geomorphology*, *318*, 336–347.